#### **OPEN ACCESS**



# Constraining Cluster Virialization Mechanism and Cosmology Using Thermal-SZselected Clusters from Future CMB Surveys

Srinivasan Raghunathan 30, Nathan Whitehorn 30, Marcelo A. Alvarez 4,50, Han Aung 9, Nicholas Battagli 40, Gilbert P. Holder, Daisuke Nagato, Elena Pierpaolo, Christian L. Reichard, and Joaquin D. Vieira, and Joaquin D. V <sup>2</sup> Department of Physics and Astronom**y**lichigan State University567 Wilson Road East LansingMl: 48824, ŪSA Department of Physics and Astronomyniversity of California, Los Angeles, CA 90095, USA Lawrence Berkeley National Laborator Qne Cyclotron Road Berkeley, CA 94720, USA Berkeley Center for Cosmological Physids C Berkeley, CA 94720, USA Department of Physics ale University, New Haven, CT 06520, USA Department of AstronomyCornell University,Ithaca,NY 14853, USA Astronomy Department University of Illinois at Urbana-Champaign,002 W. Green Street Urbana, IL 61801, USA Department of Physics Iniversity of Illinois Urbana-Champaigri,110 W. Green Street Urbana, IL 61801, USA Physics & Astronomy Department/Iniversity of Southern Californial os Angeles CA, 90089-0484 USA

11 School of Physics University of Melbourne Parkville, VIC 3010, Australia Received 2021 July 23; revised 2021 December 26; accepted 2021 December 27; published 2022 February 22

#### Abstract

We forecast the number of galaxy clusters that can be detected via the thermal Sunyaev-Zel'dovich (tSZ) signals by future cosmic microwave background (CMB) experiments; imarily the wide area survey of the CMB-S4 experiment but also CMB-S4's smaller de-lensing survey and the proposed CMB-HD experiment. We predict that CMB-S4 will detect 75,000 clusters with its wide survey of and 14,000 clusters with its deep survey of f<sub>sky</sub> = 3%. Of these, approximately 1350 clusters will be at z 2, a regime that is difficult to probe by optical or X-ray surveys. We assume CMB-HD will survey the same sky as the S4-Wide, and find that CMB-HD will detect three times more overalland an order of magnitude more z 2 clusters than CMB-S7 hese results include galactic and extragalactic foregrounds along with atmospheric and instrumental noise. Using CMB-cluster lensing to calibrate the cluster tSZ-massscaling relation, we combine cluster counts with primary CMB to obtain cosmological constraints for a two-parameter extension of the standard model (ΛCDM ₩∑mln addition to constraining  $\sigma(\mathbf{w})$  to  $\Box 1\%$ , we find that both surveys can enable a ~2.5–4.5 $\sigma$  detection of  $\Sigma$ msubstantially strengthening CMB-only constraints we also study the evolution of the intracluster medium by modeling the cluster virialization v(z) and find tight constraints from CMB-S4, with further factors of three to four improvement for CMB-HD.

Unified Astronomy Thesaurus concepts: Cosmology (343); Cosmic microwave background radiation (322); Sunyaev-Zeldovich effect (1654); Galaxy clusters (584)

#### 1. Introduction

Galaxy clusters are the largestand most massive gravitationally bound systems in the universe. They form on the densest points of the cosmic web and hence contain a wealth of information about structure formation. Specifically cluster to CMB photons through inverse Compton scatteringaev & information about structure formation. Specifically, cluster abundance as a function of mass and redshifts sensitive to cosmological parameters that govern the geometry and structure growth in the universeOf further importance is the different degeneracydirections between structure growth background (CMB) or baryonic acoustic oscillations, which provide compelling joint constraints. This has been demonstrated previously in the literature (for example Mantz et al. 2008; Vikhlinin et al. 2009; Rozo et al. 2010; von der Linden et al. 2014; de Haan etal. 2016; Salvatiet al. 2018; Bocquet et al. 2019; Zubeldia & Challinor 2019; Planck Collaboration et al. 2020a), and the potential of clusters as cosmological probes from future surveys has also been a subject of extensi study (for example, Holder et al. 2001; Lima & Hu 2004;

Original content from this work may be used under the terms of the Creative Commons Attribution 4.0 licence. Any further distribution of this work must maintain attribution to the author(s) and the title of the work, journal citation and DOI.

Sartoris et al. 2012; Mak & Pierpaoli 2013, and recently Louis & Alonso 2017; Madhavacheril et al. 2017; Cromer et al. 2019; Gupta et al.2020).

Zel'dovich 1970). This thermal Sunyaev–Zeldovich effe(ttSZ) has been used to detect clusters from CMB surveys (Bleem et al. 2015; Planck Collaboration et al. 2016a; Hilton et al. 2018, 2021; Huang et al. 2020; Bleem et al. 2020), and the number of clusters parameters probed by clusters compared to cosmic microwave has been rapidly growing from a few hundreds to thousands with the increase in sensitivity of he CMB surveys (Benson et al. 2014; Henderson et al. 2016; Bender et al. 2018). Future CMB surveys like CMB-HD (Sehgal et 2019), CMB-S4 (CMB-S4 Collaboration 2019), Cosmic Origin Explorer (CORE; Melin et al. 2018b), and Simons Observatory (SO); de et al. 2019) will increase the sample size severally, producing mass-limited cluster catalogs down to M  $_{500c}$   $10^4 M_e$ . In the context of galaxy clusters, future CMB surveys play an important and unique role as they open the window to the high redshift  $z \square 2$  universe using the redshift independent tSZ effect, enabling the detection of distantclusters. These distant lusters will otherwise be hard to detect using optical or X-ray surveys, and as a result, future tSZselected cluster samples will be complementary to the ones from Large Synoptic Survey Telescope (LSSTthetVera C.Rubin

Observatory (LSST Science Collaborationaet 2009), Euclid (Laureijs et al. 2011), and eROSITA (Merloni et al. 2012).

The clusters also gravitationally lens the background CMB. an effectknown as CMB-cluster lensing After the first set of detections using the CMB temperature by the Atacama Cosmology Telescope(ACT; Madhavacherilet al. 2015), South Pole Telescope (SPTBaxter et al. 2015), and Planck (Melin & Bartlett 2015; Planck Collaboration et al. 2016b), the the baseline results including cluster detection sensitivity, field has rapidly evolved to use the signal to calibrate richness-survey completenes and cluster counts The modification to Geach & Peacock 2017) and to warrathe first polarizationonly detection of the signalby SPTpol survey (Raghunathan et al. 2019b). Like the tSZ effect, CMB-clusterlensing also plays a key role in facilitating the mass measurements of distartoreground signals in Section 3.6 and finally conclude in clusters expected from future CMB surveys is difficult with galaxy weak lensing since the signal-to-noise ratio (S/N) of lensed background galaxies drops significantly at high redshifts. Planck Collaboration et al. (2016b) and Zubeldia & Challinor (2019) used CMB-cluster lensing information to derive cosmological constraints with the Planck cluster sample, critical density of the universe at the cluster redshift. while Alonso et al. (2016) and Madhavacherilet al. (2017) studied the potential CMB-cluster lensing either independently or in combination with galaxy weak lensing to calibrate the observable-mas $(Y_{sz} - M)$  scaling relations of clusters from CMB-S4 and its impact on cluster cosmology. While extensive studieshighlighting the importance of clusters as cosmologicalprobes existin the literature, understanding the virialization mechanism and astrophysics of high redshift 2) clusters mostly remains an unexplored territory owing to the lack of observations.

primary focus is on the wide area survey (S4-Wide) of the CMB cosmology (Planck Collaboration et al016c) obtained using S4 experiment, but we also provide predictions for the smaller but MB (Lewis et al. 2000) software. The cluster tSZ signals deeper CMB-S4 de-lensing survey (S4-Ultra deep). The proposed using a generalized Navarro–Frenk–WhiteNFW; CMB-HD experiment is also added to the list as an ideal case. We warro et al. 1996; Zhao 1996; Nagai et al. 2007a; Arnaud start by forecasting the number tSZ-selected galaxy clusters from the three survey the simulations used for forecasting are designed to capture most of the effects expected in a real survey. The simulated maps are then convolved by They contain atmospheric and instrumentabise along with signals from galactic and astrophysical foregrounds. The detected 1). Finally, we add noise realizations to the simulated clusters are then binned in lensing mass (obtained using CMB-maps. We model the noise spectra to include both atmospheric cluster lensing), tSZ S/N q, and redshift. We combine the binned instrumental noise as (Tegmark 1997) cluster counts N(AML, q) with primary CMB temperature and polarization spectra to derive parameter constraints. In addition to cosmology and the  $\mathcal{E}_{sz}$  - M scaling relation we also study the modify the tSZ signals of clusters, using two parameterizations of the virialization mode  $(Z) = 1 - \frac{Y_{cht}}{Y_{tot}}$  where  $Y_{cht}$  and  $Y_{tht}$  are the thermaland nonthermacomponents; espectively of the total integrated Compton visited  $Y_{cht}$  and  $Y_{cht}$  are the thermaland nonthermacomponents; espectively of the total integrated Compton visited  $Y_{cht}$  and  $Y_{cht}$  are the total integrated Compton visited  $Y_{cht}$  and  $Y_{cht}$  are the total integrated Compton visited  $Y_{cht}$  and  $Y_{cht}$  are the total integrated  $Y_{cht}$  and  $Y_{cht}$  are the tota evolution of the ICM using high redshiftlustersFor this, we integrated Compton-y signal  $Y_{tot} = Y_{th} + Y_{nth}$  In the first approachie use a linear mode to scale the tSZ signals from 2We note that this toy model with a step clusters with z 2 is over-simplistic for accurately capturing the function atz redshift dependence f the cluster virialization process. For example Fakhouri et al(2010) showed that mergewhich are considered an important source of nonthermal pressureses as a function of redshiftwhich would modify the virialization mechanism of high redshift clusters. To take this into account, build a second more realistic modelsing a fitting formalism,  $v(Z) = A_v \ln(1 + Z) + B_v$ , that has been derived using the analytic modelof the nonthermalpressure in the ICM (Shi&

Komatsu 2014Green etal. 2020) and tested using Omega500 simulations (Nelson et al. 2014a; Shi et al. 2015).

This paper is structured as follows: We describe the simulation componentscluster virialization model, detection algorithm, mass calibration using CMB lensing, and the Fisher formalism to combine binned cluster counts with primary CMB information in Section 2.In Sections 3.1 and 3.2we discuss mass scaling relations of optically selected galaxy clusters (e.gc, luster sensitivity and counts due to changes in the virialization mechanism are given in Section 3.3.We discuss the Fisher forecasts along with the impact of several choices we make in Sections 3.4 and 3.5.We test the effect of cluster correlated Section 4.

> Throughout this work, we use Planck 2015 cosmology (TT+ lowP in Table 4 of Planck Collaboration et al. 2016c) and report cluster masses in units of M which is the mass within a sphere of radius  $R_{500c}$  where the density is 500 times the

# 2. Methods

#### 2.1. Simulations

The simulations used for this study are 2° × 2° wide CMB temperature realizations with a pixeesolution of Q'5. Other than primary CMB, the simulations also contain the following frequency-dependerstignals: cluster tSZ, galactic and astrophysical foregrounds, and experimental noise (both atmospheric and instrumental). The underlying power spectrum In this work, we focus on astrophysicaland cosmological constraints using cluster samples from future CMB surveys. Our spectrum for the fiducial Planck 2015 et al. 2010) profile as described below in Section 2.4. Galactic and astrophysical foreground modelings are presented in ĕxperimentalbeam functions, assumed to be Gaussian (see

$$N_{\ell} = D_T^2 \left[ 1 + \frac{\ell}{\ell_{\text{knee}}} \right]^{a_{\text{knee}}},$$
 (1)

being affected by the atmospheric (ℓ ≰rfee) and instrumental noise components ( $\ell_{kn}$ ).

# 2.2. Experimental Setup

We consider three future CMB surveys in this work: CMB-HD, S4-Wide, and S4-Ultra deep. Table 1 lists the instrumental noise levels D<sub>T</sub> (mK - arcmin) and experimentalbeams of each frequency band fothe three surveysCMB-HD is a proposed wigh-resolution millimeter-wave survey scanning large regions of the sky from Chile with a 30 m primary mirror and designed to operate in seven bands from 30–350 GHz (Sehgal et al. 2019, 2020). CMB-S4 is an upcoming survey that currently

Table 1 **Experimental Specifications** 

Experiment	Location ( § <sub>ky</sub> )	Beam ∯ <sub>WHM</sub> [arcminutes]					$\Delta_{T}[mK$ - arcmin								
		30	40	90	150	220	270	350	30	40	90	150	220	270	350
CMB-HD	Chile (67%)	1.4	1.05	0.45	0.25	0.20	0.15	0.12	6.5	3.4	0.73	0.79	2.0	2.7	100
S4-Wide		7.3	5.5	2.3	1.5	1.0	0.8	K	21.8	12.4	2.0	2.0	6.9	16.7	K
S4-Ultra deep	South Pole (3%)	8.4	5.8	2.5	1.6	1.1	1.0	K	4.6	2.94	0.45	0.41	1.29	3.07	K

in its design stages and expected to stamperations latethis decade (CMB-S4 Collaboration 2019) this work, we only consider the two CMB-S4 large aperture telescope surveys an not the small aperture telescope survey that aimed at the inflationary gravitational aves. The two S4-LAT surveys (S4-Wide and S4-Ultra deep)will be performed using 6 m class telescopes in six frequency bands from 30 to 270 GHzS4-Wide is a legacy survey from Chile and will cover roughly 67% of the sky area. S4-Ultra deep is the "de-lensing" survey that is aiming to provide deep observations of ~3% of the sky from the South Pole. The primary objective of the S4-Ultra deep survey is to generate high-resolution maps of the dark matter distribution in the universe to facilitate the detection of inflationary B-modes by cleaning the lensing-induced B-modes However, given the large telescope size, S4-Ultra deep also has the capability to detect high redshift SZ clusters, as we show in Gaussianities. Other galactic signals like free-free and this work. The parameters governing the atmospheric 1/f noiseanomalous microwave emissions, which should have a  $\ell_{\text{knee}}$  and  $\alpha_{\text{knee}}$  are listed in Table 2 (CMB-S4 Collaboration 2019). For simplicity, we assume the 1/fmodel and sky fraction for CMB-HD to be the same as those in the Chile-

# 2.3. Foreground Signals

based S4-Wide survey.

Although extragalactic foregroundsemissions from dusty star-forming galaxies (DSFGs) in particular, are expected to be ange -45° \_ b \_ -30 We compute the temperature power the major source of contamination for cluster detection, the footprint of Chile-based experiments cover 67% of the sky areaegions for all of the frequency bands of interest. and will be subjected to contamination from galactic emission. signals for CMB-HD and S4-Wide. For S4-Ultra deep, we only galactic signals in the remaining 77% (fsky = 50%) to be include extragalactic foregrounds, as it will observe a relatively similar to the low emission region. As is evident from the clean region of the sky shown as the yellow dashed contours infigure, the blue contours do not correspond to the cleanest Figure 1.

# 2.3.1. Galactic Emission

The galactic foreground signals dust and synchrotron are position dependentand hence one cannotrely on Gaussian realizations of an underlying power spectrum for the entire footprint. To this end, we use the publicly available pySM3 dust and synchrotron map simulations, which were built specifically in the context of CMB-S4For more details about pySM3 simulations, we refer the reader to the originalwork (Thorne et al.2017), which is partly based on the Planck Sky S0\_s0 synchrotron models of pySM where the dustemperature, dust emissivity index, and synchrotron spectral index do Ultra deep lies in a relatively clean region do not include not have spatialvariations. The models also ignore any non-

Table 2 Atmospheric 1/f Noise Specifications (Lee akne)

nd Band [GHz]	CMB-HD	S4-Wide	S4-Ultra deep		
30	471,	3.5	1200,4.2		
40	478,	1200,4.2			
<sub>6</sub> 90	2154	,3.5	1200,4.2		
is <sub>150</sub>	4364	1900,4.1			
220	7334	2100,3.9			
270	7308,3.5				
es <sup>350</sup>	7500,3.5	L	L		
. :=					

negligible impact on cluster searches, are ignored in this work. To estimate the position-dependental actic foregrounds we first divide the S4-Wide footprint into two high and low emission regions, shown as the red and blue contours in Figure 1. The high emission region corresponds to ±15° and encompasses most the signals from the galactic plane. The low emission region corresponds to regions in the spectra  $C_{pal}^{gal}$  of dust and synchrotron signals of both these

We assume 23% ( $_{s}f_{v}$ = 17%) of the S4-Wide footprint to Hence, we consider both galactic and extragalactic foregroundhave galactic signals similar to the high emission region and the region in the S4-Wide footprint, and hence this is a conservative choice. With this assumption, we use the  $C_\ell^{\rm gal}$ spectra estimated in the two regions to generate Gaussian realizations of galactic emission and add them to our maps to produce two sets of simulated skies. The underlying power spectrum for the other signals in the two sets is the sarBy. doing this, we approximate the galactic powespectra to be constant inside the two region\$Ve validated this assumption by dividing the S4-Wide footprint into six regions (latitude steps of  $\Delta b = 15^{\circ}$ ) with different galactic emission and do not find a significant difference in the number of detected clusters Model code (Delabrouille et al. 2013). We use S0\_d0 dust and between the two approaches. We follow the same approach for CMB-HD. Like mentioned above since the footprint of S4galactic foregrounds for S4-Ultra deep simulations.

The CMB-S4 pySM3 simulations do not include the 12 S4-Ultra deep is also expected to have a 20 GHz band, but we ignore that in 350 GHz band, which is required for CMB-HD. We obtain auto-spectra of the galactic dust the 350 GHz band and its cross correlation with other bands by simply scaling the

this work for simplicity.

<sup>&</sup>lt;sup>13</sup> https://github.com/CMB-S4/s4mapbasedsims/tree/master/202102\_ design\_tool\_input

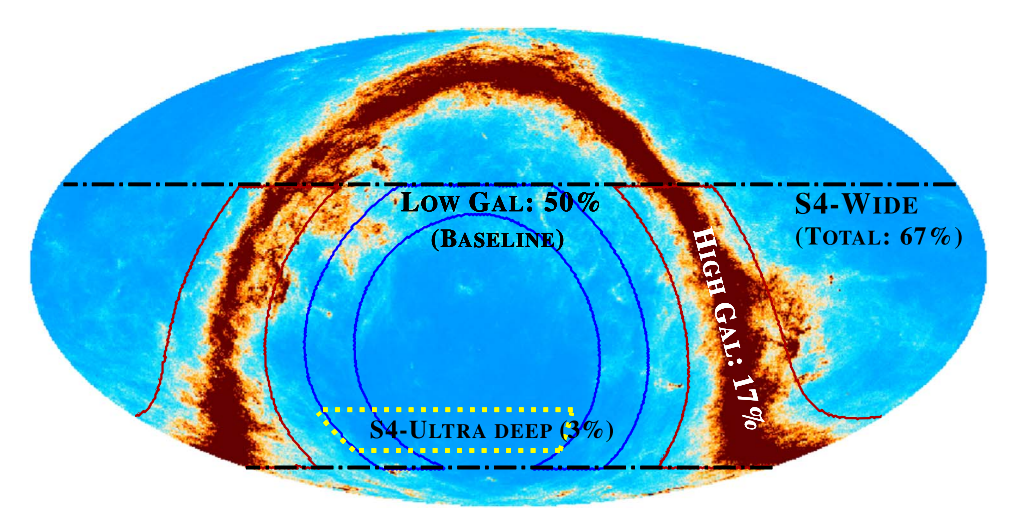


Figure 1. Map of the galactic dust emission at 150 GHz from pySM3 simulations. The expected footprints for S4, Wie 67%) and S4-Ultra deep (kf = 3%) are highlighted in black and yellow. Regions of high and low galactic emissions used for injecting galactic foregrounds in our simulations are marked as red and bli contours. We assume the galactic emission in 23% of the S4-Wide footprint1(7%) to be similar to high galactic emission in the red contours and the emission in the remaining 77% ( t,t = 50%) to be similar to low galactic emission in the blue contours (marked as baseline). This is a conservative choice as the blue contours a not the cleanest region in the S4-Wide footprint. We use the same S4-Wide footprint and strategy for CMB-HD. Since S4-Ultra deep will observe in a relatively clear patch, we do not include galactic foregrounds for S4-Ultra deep simulations.

# 270 GHz dust spectra as

$$C_{\ell, n_1 n_2}^{\text{gal-dust}} = C_{\ell, n_0 n_0} \, \mathbb{I}_{n_1, n_2} \, \frac{h_{n_1} h_{n_2}}{h_{n_0} h_{n_0}}, \tag{2}$$

where  $v_0 = 270$  GHz and  $v_1$ ,  $v_2$  ä[30, 40, 90, 150, 220, 270, 353] GHz. The terms, and n in Equation (2) when combined represent the spectral energy distribution \$ED) of dust, and we use a modified blackbody of the form

$$h_n = n^{b_0} B_n \mathcal{T}_{g} \tag{3}$$

and

 $T_{CMB}$  = 2.73 K, emissivity index  $\beta_d$  = 1.6, and dust temperature T<sub>d</sub> = 19.6 K, similar to pySM3 simulations that are tion et al. 2020b). We ignore synchrotron signals 250 GHz since they are expected to be negligible compared to dust such high frequencies.

#### 2.3.2. Extragalactic Foregrounds

Diffuse extragalactic foreground signatin be decomposed into: emissions from DSFGs and radio galaxies (RGs) below the detection threshold; and kinetic SZ (kSZ) and tSZ signals. Note that DSFGs are responsible forcosmic infrared background (CIB) anisotropies atmillimeter/submillimeter waveinterchangeably in this workDSFG and RG signals were all modeled as Gaussian realizations using SPT power spectra observationsmasked DSFGs and RGs detected above5σ, which corresponds a flux threshold of S<sub>150</sub>~6 mJy. However, the 5σ detection limit for the future surveys considered here wilbe much lower: S<sub>150</sub>~ 2 mJy for CMB-

S4 (CMB-S4 Collaboration 2019) and \_\_0.1 mJy for CMB-HD (Sehgalet al. 2019). For CMB-S4, we do not modify the masking threshold and simply use SPT measurementsus, DSFG and RG signals injected into S4-Wide and S4-Ultra deep simulations are conservative estimateFor CMB-HD, however, Sehgalet al. (2019) claim that sources with flux above 0.04 mJy can be efficiently removed by detecting them  $3\sigma$  in the 270/350 GHz bands. This lowers the DSFG power in 150 GHz by ×17, and we adopt that strategy here. The masking threshold for RG is not modified from SPT values. The frequency dependence of DSFG and RG signals is also adopted from SPT (George et al. 2015; Reichardtet al. 2021) measurements. We introduce decorrelation in the DSFG signals between the 270/350 GHz and 150 GHz bands using SPT × Herschel/Spectraland Photometric Imaging Receiver (SPIRE) measurements (Viero et al. 2019). We estimate the B<sub>v</sub>(T) in the above equations is the Planck function, and we set correlation coefficient between the 150 GHz and 270/350 GHz bands by interpolating the values in Table 1 of Viero et al. (2019).

The kSZ signal is contributed to by two distinct sources: one consistent with measurements from Planck (Planck Collabora-from the Doppler boosting of CMB photons due to the motion of haloes and the other from the epoch of reionization. We use the Reichardtet al. (2021) measurement simulate the kSZ signal. This roughly corresponds to flaspectrum in Q with  $D_{\ell,3000}$  = 3  $\mu\text{K}^2$  where  $D_{\ell}=C_{\ell}\,\frac{\ell\,\ell\,+\,1)}{2p}$  and has no frequency dependence. For the diffuse tSZ, we consider power from all haloes with  $M_{500c}$   $10^3 M_e$ , modeled using the Arnaud profile (Arnaud et al. 2010), in the redshift range z ä [0.1, 4.0]. Both the diffuse kSZ and tSZ signals are simulated as Gaussian realizations using the respective power spectra described above.

lengths, and we sometimes use the two terms, DSFGs and CIB, In our fiducial setup, DSFG/RG/kSZ signals are assumed to be uncorrelated to the cluster under study. This is, however, not entirely correct as galaxies preferentially reside inside clusters, measurements (George et al. 2015; Reichardt et al. 2021). SPand the cluster motion can also give rise to kSZ signals. We test this assumption in Section 3.6 by injecting cluster correlated foreground signals using Websky (Stein et al. 2020) and MultiDark Planck 2 (MDPL2,Y. Omori 2022, in preparation) simulations.

### 2.4. Cluster tSZ Signal

We model the ICM pressure using the dimensionless universal pressure profile P<sub>e</sub>(x) proposed by Nagai et al. (2007a) and calibrated using X-ray observations by Arnaud et al. (2010)

$$P_{e}(\cdot, X) = \frac{P_{0}}{(C_{500}X)^{g}[1 + (C_{500}X)^{a}]^{\frac{b-g}{a}}},$$
 (5)

where the distance to the cluster center x ₹0% Pexpressed in terms of virial radius 🖧 and concentration parameteroare related to scale radius  $\xi$  as  $x = r/r_s$  and  $c_{500} = R_{500}/r_s$ . The best-fit values of the parameters are (Arnaud et al. 2010):  $c_{500}\text{=}\text{ 1.177, the normalization constant}=8.403\ h_{70}^{3/2}\text{, and}$ the exponents are  $\alpha = 1.0510$ ,  $\beta = 5.4905$ , and  $\gamma = 0.3081$ . The pressure profile  $\mathbb{R}$ , x) is integrated along the line of sight to obtain the Compton-y signal y(x) as

$$y(X) = \frac{s_T}{m_e c^2} \grave{Q} P_e (x, X) dI$$
 (6)

and is converted into CMB temperature units as

$$d\tau = Y(X) g_{SZ}(n) T_{CMB} K, (7)$$

where  $\sigma_T$  in the Thomson cross sections is the velocity of light,  $m_e$  is the electron mass,  $T_{CMB}$  = 2.73 K is the mean temperature of the CMB, and g<sub>SZ</sub>(v) is the frequency dependence of the tSZ signal/which, ignoring relativistic SZ corrections (e.g., Itoh et al. 1998; Chluba et al. 2012), is given by

$$g_{SZ}(n) = X \coth(X/2) - 4; X = \frac{h_n}{k_B T_{CMB}},$$
 (8)

where h and k<sub>B</sub> are Planck and Boltzmann constants, respectively.

We integrate y(x) over the angular extent of the clusteroR to obtain the total integrated clusterCompton  $Y_{\text{SZ}_{5000}}$  defined to obtain the total integrated clusterCompton  $r_{SZ_{5000}}$  defined the virialization efficiency of clusters that modifies the tSZ using Planck Collaboration et al. (2016b) but generalized based signal of clusters using a linear scaling as on Alonso et al. (2016) and Madhavacherilet al. (2017) to include mass and redshift evolution as

$$Y_{SZ_{500c}} = V(Z) Y_{\star} \left[ \frac{h}{0.7} \right]^{\frac{2}{3}} \left[ \frac{M_{500c}}{M_{\star}} \right]^{a_{Y}} \left[ \frac{M_{500c}}{M_{\star}} \right]^{a_{Y}} e^{b_{Y} \log^{2} \left( \frac{M_{500c}}{M_{\star}} \right)} \left[ \frac{D_{A(Y)}}{100 \text{ Mpc}} \right]^{2} E^{2/3} (Z) (1 + Z)^{g_{Y}},$$
 (9)

where  $M_* = 6 \times 10^{14} M_e$  is the pivotal mass,  $D_A(z)$  is the angular diameter distance to the cluster at redshift z,  $E(z) = H(z)/H_0$  is the Hubble function, and  $M_{500c}$  is the mass of the cluster. v(z) in the above equation is the cluster virialization model adopted to modify the cluster tSZ signal and parameterize the redshift dependence of the virialization is explained below in Section 2.5. We use Planck Collaboration process (e.g. Fakhouri et al. 2010) more accurately in this et al. (2016b) best-fit values to fix  $\log Y_* = -0.19$  and  $a_v = 1.79$ . The fiducial values for redshift g<sub>v</sub> and second-

include mass and redshift evolution as

$$s_{\log Y}(M_{500c}, Z) = s_{\log Y, 0} \left[ \frac{M_{500c}}{M_{\star}} \right]^{a_s} (1 + Z)^{g_s}$$
 (10)

with the fiducial values set to  $s_{log} Y_{,0} = 0.127$ ,  $\alpha_{\sigma} = 0$ , and  $\gamma_{\sigma}$  = 0 (Louis & Alonso 2017).

# 2.5. Modeling the Cluster Virialization

Not much is known about the astrophysics of high redshift clusters owing to the lack of sufficient observationsLately, Mantz et al. (2014) and Mantz et al. (2018) used Combined Array for Research in Millimeter-wave Astronomy (CARMA) data to perform detailed tSZ study of a distant cluster at  $Z = 1.99^{+0.19}_{-0.21}$  with  $M_{500c} \sim 1 - 2 \times 10^{14} M_e$  that was detected by the X-ray XMM-Newton satellite. Mantz et al. (2018) report that the properties of this distant cluster are in reasonable agreementwith the extrapolated scaling relations confirming self-similar evolution of clusters out to  $z \sim 2$ . However, the authors also caution the readers abogeneralizing the result from a single z ~ 2 cluster to all high redshift clusterAs we will see later in Section 3.2CMB-HD and CMB-S4 have the capability to detect hundredsto thousands of clusters with  $M_{500c} \square 10^4 M_e$  at z  $\square$  2Subsequentlywe aim to study the physics of the ICM and its evolution out to high redshifts with these potential detections. To this end, we tweak the first term in Equation (9),  $V(Z)^{\circ}$   $\left[1 - \frac{Y_{\text{non-th}}}{Y_{\text{tot}}}\right]$  that controls cluster virialization and as a result modifies the cluster tSZ signal. We model v(z) in two different ways as described below.

# 2.5.1. Linear Scaling: Model 1

In the first approachie use a simple model

$$V(\bar{Z}) = h_{\nu}(\bar{Z}) (1 - b_{\mu s E})^{a_{\gamma}},$$
 (11)

where b<sub>HSE</sub> is the hydrostatic equilibrium (HSE) mass bias set to  $b_{\text{\tiny HSE}} = 0.2$  (Zubeldia & Challinor 2019; Makiya et al. 2020) and assumed to be constant for clusters at all redshifts) is

$$h_{v}(\overline{z}) = \begin{cases} 1, \, z < 2 \\ 1 + \mathbb{I}, \, z \mathbb{I} & 2 \end{cases} \tag{12}$$

with  $\grave{o}$  ä [-1, 1]. This model is similar to the  $M_{SZ}$  - M relation used in Planck Collaboration et al. (2016b) except for the introduction of  $\eta_i(z)$  for high-z clusters. The fiducial value of  $\eta_{v}(z) = 1$  for all clusters.

## 2.5.2. Physically Motivated Model 2

Since the step function at 2 used in the above model highly simplistic, we now build a realistic model to second approaching use the analytic modelor modeling the evolution of the nonthermal pressurefraction through the cluster assembly and virialization processes (Statial. 2015) and their impact on the  $Y_{sz}$  - M relation of high redshift clusters using the model presented in Green et(aD20). We summarize the modeling and results in the Appendix, in which we use a fitting formalism

$$v(Z) = A_v \ln(1 + Z) + B_v \tag{13}$$

& Komatsu 2014; Green et al. 2020) and tested using the Omega500 hydrodynamicadosmologicalsimulation (Nelson et al. 2014a; Shi et al. 2015). We set the fiducial values of the parameters to be  $\neq$  0.155 and B = 0.189.

#### 2.6. Cluster Detection

We combine the simulated maps in different frequency channels Nh optimally using an internal linear combination (ILC) algorithm and create a Compton-y map as

$$Y_{\ell} = \mathop{\mathbf{a}}_{i=1}^{N_{ch}} w_{\ell}^{j} M_{\ell}^{j}, \tag{14}$$

where the multipole-dependenteights w for each frequency channelare computed using the SMICA (SpectraMatching IndependentComponentAnalysis) algorithm (Cardoso etal. 2008; Remazeilleset al. 2011; Planck Collaboration et al. 2014) as

$$W_{\ell} = \frac{C_{\bar{\ell}}^{-1}a}{a^{T}C_{\bar{\ell}}^{-1}a}.$$
 (15)

The matrix  $C_{\ell}$  has a dimension  $N_{th} \times N_{ch}$  and contains the given multipole  $\ell$ . The frequency response vector  $\mathbf{a} = [-5.33]$ -5.23, -4.36, -2.61, 0.09, 2.27, 5.95] contains the tSZ spectrum given in Equation (8) for [30, 40, 90, 150, 220, 270, 350] GHz channels. The weights in Equation (15) for each band are chosen optimally to produce a minimum variance Compton-y map by jointly minimizing the contamination from the noise and foreground signals that are uncorrelated with the best-fit lensing masses. In the inpainted-gradientQE, we cluster. We do not explicitly null any foreground components using a constrained ILC technique (Remazeilles ætt 2011), but study the effect of cluster correlated foreground signals in Section 3.6.

### 2.6.1. Maximum Likelihood Approach

The resultant ILC Compton-y map is then used to compute the S/N of the cluster tSZ signal using a maximum likelihoodbased approach or blind cluster searchespwever, adopting a multiband matched-filtering technique (Melin etal. 2006) would be computationally more feasible as done traditionally in cluster finding using CMB surveys (e.g. Bleem et al. 2015). The two approaches are equivalent addition to the cluster tSZ signal, this map includes variance from diffuse tSZ and also the residualCMB, foreground signals and noise. Using this 2° × 2° ILC y map, we calculate

$$-2 \ln \mathbb{I} = \mathring{\mathbf{a}}_{ij} (\mathbf{y}_{i} - \mathbf{y}_{i}^{th}) C_{ij}^{-1} (\mathbf{y}_{j} - \mathbf{y}_{j}^{th}), \tag{16}$$

where  $y_i \equiv y_i(\theta)$  is the azimuthally averaged profile of the Compton-y signalin bins i of  $\Delta\theta$  = 0.5, out to a maximum  $q_{\text{max}} = 2 \hat{x}$ . The chosen  $q_{\text{max}}$  encompasses the tSZ sign farbm the majority of the clusters at all redshifts and hence maximizes number counts in a given  $bN_{Z_i}$ ,  $M_{L_i}$ ,  $q_k$ )  $\circ$   $N_{Z_i}$ ,  $Q_k$ the S/N. Specifically,  $q_{\text{max}} \square q_{5000}$  for clusters with z  $\square$  0.5

where  $\theta_{500c}$ =  $R_{500c}/D_A(z)$  and  $D_A(z)$ . The measured cluster Compton-y from a cluster with a given mass and redshift is We compute theory models yth for different massesat the derived from the analytical model of nonthermal pressure (Shi cluster redshift using Equation (9) and fit them to the measured y signal. The covariance matri € includes contribution from other sources of variance described above. It is computed using N = 2500 simulations as

$$C = \frac{1}{N - 1} \mathring{\mathbf{a}}_{n-1}^{N} (\mathbf{y}_{i} - \acute{\mathbf{a}} \mathbf{y} \tilde{\mathbf{n}}) (\mathbf{y}_{i} - \acute{\mathbf{a}} \mathbf{y} \tilde{\mathbf{n}})^{T}. \tag{17}$$

We use the distribution of best fits recovered from 100 simulations and compute the S/N as the inverse of the 1\sigma uncertainty defined by the 16% to 84% confidence range. For each survey, we compute an S/N look-up table in this way for different clusters in an ( $M_{500e}$  z) grid:  $\log M_{500e} \hat{1}$  [13, 15.4]  $M_{\Box}$  with  $\log DM = 0.1 M_{\Box}$  and z ä [0.1,3] with  $\Delta z = 0.1$ . This S/N look-up table is used to select clusters above the detection threshold  $S/N \equiv q = 5$  in later sections.

### 2.7. Mass Calibration Using CMB Lensing

We perform internal mass calibration of clusters using their gravitational lensing signatures on both CMB temperature and polarization anisotropies. Cluster kSZ and tSZ signals are expected to introduce significant bias to temperature-based covariance between simulated maps in multiple frequencies at Ansing reconstruction (Raghunathan et al. 2017). We mitigate them by employing an inpainted-gradie (Raghunathan eal. 2019a) quadratic temperature lensing estimator (QE; Hu et al. 2007). This estimatorreconstructs lensing using the lensinginduced correlations between a large-scale and a small-scale temperature anisotropies map. Cluster SZ signals, in addition to lensing, can also introduce such correlations, which tend to bias remove SZ signals in the large-scale gradient map by estimating the pixel values at the cluster location using information from adjacent pixels or polarization, we use the optimal maximum likelihood estimator (MLE; Raghunathan et al. 2017), which reconstructs cluster massesusing the lensing-induced changes to a pixel-pixel covariance matrix. We ignore the covariance between temperature and polarization but note that it can slightly degrade the lensing S/N.

#### 2.8. Fisher Formalism

We use the Fisher matrix formalism (Holder et al. 2001) and compute

$$F_{q,q} = \mathring{a}_{z,M_{L}q} \frac{\P^{N(Z,M_{L}q)} - \P^{N(Z,M_{L}q)}}{\P^{q}} \frac{1}{\P^{q}} \frac{1}{N(Z,M_{L}q)}, \quad (18)$$

where  $\theta \theta$  are the astrophysical or cosmological parameters to be constrained; N(zLMt) is the number of clusters in a given lensing mass M, tSZ S/N q, and redshift z bin; and 1/N(z, M) gives the Poisson error in each bin. The summation indices lgz run over the M., g. and z bins described below in Section 2.8CAuster be calculated as

$$NZ_{i}, M_{L_{j}}, q_{k}) = \grave{O}_{Z_{i}}^{Z_{i+1}} dZ \grave{O}_{M_{L_{j}}}^{M_{L_{j+1}}}$$

$$' dM_{L} \grave{O}_{q_{k}}^{q_{k+1}} dQ \grave{O}_{0}^{*} dMdY_{SZ} \frac{dV}{dZ_{true}dW}$$

$$' n(M, Z_{true}) \square (A, Z_{true}, S_{Z}) \square (M_{L}M, S_{M_{L}})$$

$$' \square (Q|Y_{SZ}/SY_{SZ}, 1)$$

$$' \square (\log Y_{SZ}|M, Z_{true}, S_{\log Y_{SZ}}), \qquad (19)$$

where  $n(M_{5000} z_{true}) \equiv n(M, z_{true})$  is the Tinker et al. (2008) halo mass function (HMF)and  $\frac{dV}{dz_{true}dW}$  is the volume element. We parameterize the probability density functions (PDFof redshift z, lensing mass  $M_L$ , and tSZ S/N q using normal distributions (m, s) with mean  $\mu$  and width  $\sigma$ . The scatter in the observable-mass scaling relation YM is parameterized using a log-normal  $\mathbb{I}(\log Y_{SZ}|M,Z_{true},s_{\log Y_{SZ}})$  with width  $s_{\log Y_{SZ}}$ . Since the photometric redshifterors for clusters from future surveys are expected to be small compared to the width Subsequentlythe weights are decomposed into w wtsz. wq, of the redshift bins described below (LSST Science Collaboration et al. 2009), we neglect redshift errors by setting  $z = \overline{r_t z}$  with  $\sigma_z = 0$ ; i.e., we assume  $(4 \ \overline{z_{rue}}, s_z)$  to be a  $\delta$  function. Errors in tSZ flux  $s_{Y_{SZ}}$  are obtained using the MLE approach described above, and the errors in lensing mass  $s_{M_i}$  are determined using CMB temperature and polarization-based reconstructions.

#### 2.8.1. Monte Carlo Sampling

We solve the above integral using a Monte Carlo (MC) sampling approach to estimate N(ML, q) and its derivatives  $\partial N(z, M_L, q)/\partial \theta$  as a function of the parameter under consideration  $\theta$ . We start by getting the number of haloes  $n(M_{5000} z)$  in the following mass and redshiftbins using the Tinker et al. (2008) HMF:  $M_{500c}$ ä [ $10^{13}$ ,  $10^{16}$ ]  $M_e$  with  $\Delta M_{500c}$ =  $10^{12}$   $M_e$  and 0.1 z 3with  $\Delta z$  = 0.1. While statistical uncertainties in the HMF parameters could be potentially important (Artis et al2021), we defer their impact on the results to a future work. For each halo, we assign a tSZ lensing power spectrumWe make a conservative choice and flux  $Y_{SZ}$  from  $\Box$  (log  $Y_{SZ}|M,Z$ ,  $s_{\log y_{SZ}}$ ) and an associated tSZ S/N q from  $\Box$  ( $q|Y_{SZ}/sy_{SZ}$ , 1). The tSZ S/N for the halo is obtained by interpolating the S/N look-up table in Section 2.6.1. Lensing mass and redshifts are also assigned using the distributions  $(M_LM, s_{M_L})$  and  $(4 \ Z_{true}, s_z)$ . Next we bin the haloes in lensing mass, S/N, and redshift to obtain binned cluster counts N(z, M<sub>L</sub>, q) as described below. We repeat the MC sampling approach 100 times to ensure the convergence of cluster counts N(1/2), q).

## 2.8.2.Binning Scheme

tSZ S/N: M ä [10<sup>12</sup>, 10<sup>16</sup>] M and q ä [5, 500]. For redshift, we could include Planck information on large scale and in the consider four different binning schemes. In the baseline case, wagions notcovered by the experiments in this worke avoid use  $\Delta z = 0.1$  for  $0.1 \pm z < 1.5$  and conservatively group all highten in the baseline setup. We also avoid adding S4-Wide While dedicated follow-up observations re needed to obtain redshifts for clusters at z in multiple LSST bands will still allow us to set a lower limit on To generatepolarized foregrounds, we assume 2% (3%)

the clusterredshifts, and we set this threshold to be z = 1.5. Redshifts of clusters with z < 1.5 can be obtained using upcoming optical and X-ray surveys (LSST Science Collaboration at 2009: Merloni et al. 2012). We also explore otherhoices for redshift binning: (i) an extremely optimistic case of  $\Delta z = 0.1$  for all clusters;(ii) a less conservative choice of  $\Delta z = 0.1$  for  $0.1 \underline{\hspace{0.2cm}}$  z < 2 and  $\Delta z$  = 1 for 2  $\underline{\hspace{0.2cm}}$  z  $\underline{\hspace{0.2cm}}$  3; and (iiia) pessimistic setting by ignoring clusters at z > 1.5.

#### 2.8.3. Derivatives ∂z,M<sub>L</sub>, q/∂θ

We estimate derivatives of binned cluster counts ∂N(4,,  $q)/\partial\theta$  as a function of parameter using a finite difference method. For this, the MC sampling approach must be repeated twice for every parameter perturbing  $\theta \rightarrow \theta \not\equiv \overline{\sigma}$  he randomness in sampling, however, can lead to unstable derivatives, and we avoid this by only estimating counts N(M, q, z) at the fiducial values of the parametersFor derivatives,we assign weights to haloes based on the ratio of the PDF at the sampled point before and after modifying the parameter values. weights ( $w_Z$ ,  $w_q$ ,  $w_{M_L}$ , and  $w_y$ ) are simply the ratio of respective individual PDFs at the sampled point  $\frac{\| (m \cdot \$)_q \|}{\| (m \cdot \$)_q \|}$  described in Section 2.8, and  $\theta$  is one of the 16 parameters being constrained: observable-masscaling relation parameter  $\{a_y, b_y, g_y\}$  in Equation (9) and  $a_{\log Y}$ ,  $a_s$ ,  $g_s$ ] in Equation (10); cosmological parameter  $A_s$ ,  $A_s$ virialization parameters from one ofthe two models, namely  $[h_{v}, b_{HSE}]$  in Equation (11) or  $[A, B_{v}]$  in Equation (13).

### 2.8.4.CMB TT/EE/TE Fisher Matrix

Along with cluster counts, we also make use of the information from primary CMB temperature and polarization power spectraSince clusters can lens the background CMB, cluster counts will have a nonzero covariancewith CMB fully ignore information from CMB lensing power spectrum in this work. We use lensed CMB spectra but not correct for the lensing-induced correlations. Because of the nonzero covariance between clusters and CMB lensinge note that this can underestimate the error bars (Green et al. 2017). However, the effect is small, and hence we do not consider it. In a similar vein, we ignore information from the tSZ power spectrum since it must be highly correlated with cluster counts.

We compute CMB Fishermatrices using TT,EE, and TE power spectra  $f_{\text{r(ax)}} = 5000$ ) obtained using CAMB (Lewis et al. 2000) software for the fiducial Planck 2015 cosmology described in Section 2.1. The CMB TT, EE, and TE information comes We choose 40 and 25 logarithmic bins for lensing mass and from the same experimentunder considerationAlthough we redshift clusters 1.5 \_ z \_ 3 in one massive redshift bin similainformation in the regions not covered by S4-Ultra deep. Like in that in Madhavacheril et al. (2017). This is due to the difficulties the case of Compton-y maps, we optimally combine information that will be encountered in measuring redshifts of distant clustefrom all frequency channels using the ILC algorithm to compute the residualnoise (see Table 1 and Table 2)and foreground 1.5, the absence of an associated signata (see Section 2.3) in the CMB maps for all three surveys.

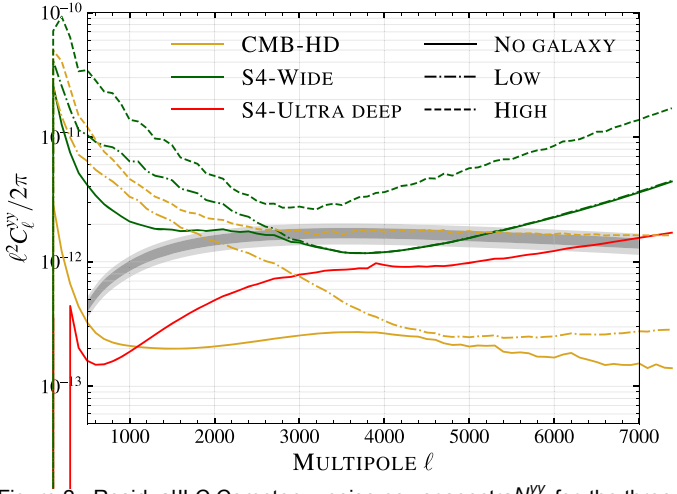


Figure 2. Residual ILC Compton-y noise power spectra  $N_\ell^{yy}$  for the three surveys: CMB-HD in yellow, S4-Wide in green, and S4-Ultra deep in red. Solid curves correspond to noise curves without the inclusion of galactic signals. Dashed-dotted and dashed lines are the residualse curves in the level of the fiducial tSZ power spectrum along with 1 $\sigma$ , 2 $\sigma$  errors from George et al. (2015). Cluster detection sensitivity for CMB-S4 will be limited by residual CIB signals, while the confusion noise from diffuse tSZ is the dominant source of variance for CMB-HD.

polarization fractionsfor dusty star-forming (radio)galaxies consistent with measurements from ACT (Datta et al. 2019) antSZ power spectrum (3000 \_\_ ℓ \_\_ 4500) with S/N SPT (Gupta et al. 2019). Diffuse kSZ and tSZ signals are assumed Collaboration 2019). to be unpolarized nformation about polarized galactic dust and synchrotron signals comes from pySM3 simulations (see Section 2.3.1).

#### 3. Results and Discussion

# 3.1. Noise Level in Compton-y Map

Figure 2 shows the residuabower in the ILC Compton-y maps  $(N_\ell^{yy})$  for CMB-HD (yellow), S4-Wide (green)and S4-Ultra deep (red). Solid lines in the figure correspond to noise estimates when galactic emission is noincluded. CMB-HD and S4-Wide experiments are expected to scan large sky areas ( $f_{sky}$ = 67%), and it is unrealistic to ignore galactic emission. Hence for CMB-HD (yellow) and S4-Wide (green) experiments, we also show the noise curves in regions of low (dashed-dotted)and high (dashed) galactic emission as discussed in Section 2.3.1Since S4-Ultra deep will observe a region with negligible galactic foregrounds (CMB-S4 Collaboration 2019)we only show a solid red line.

In the absence of galactic emission (solid curves) find the noise level in CMB-HD maps to be much lower than both S4-Wide and S4-Ultra deep surveyshis is primarily due to the reduced level of CIB signals expected in CMB-HD compared to CMB-S4. As described in Section 2.3.2, note that the CIB power at 150 GHz for CMB-HD is lower than CMB-S4 by 17× (Sehgalet al. 2019). The Compton-y maps from CMB-S4 are fully dominated by residual CIB signals on small scalesResidual CIB signals in Compton-y maps can be lowered by nulling CIB signals assuming one or more spectral S4-Ultra deep and S4-Wide survey\$he dominantsource of energy distributions with a constrained ILC (Madhavacheril et al. 2020) or using partial ILC techniques (Bleem et al. 2022) contamination present the ILC maps on small scales. We This CIB reduction comes at the cost of higher noise depending weaked CMB-S4's configuration to investigate if the residual on the choice of cleaning. We ignore this here butstudy the systematics in the recovered cluster tSZ signals due to

emissions from DSFGs within clusters (tSZ × CIB) in Section 3.6.

On large scaleswe note a change in noise trend and find noise in CMB-HD to be slightly higher than S4-Ultra deep. This is due to a higher atmospheric noise in CMB-HDas it will be located in Chile (Sehgaet al. 2020) compared to S4-Ultra deep, which will be observing from the South PoleFor S4-Wide, both atmospheric noise and residua MB signals dominate the large-scale noise, which is much higher than both CMB-HD and S4-Ultra deep surveys. Including information from Planck will improve the noise performance on large scales, but we ignore that as we are primarily interested in  $\ell \square$  3000 for cluster detection.

When galactic emission is included as expected the noise increases forboth CMB-HD and S4-Wide surveys. For S4-Wide, adding low levels of galactic emission (blue contour in Figure 1) only affects large-scale noise (green dashed-dotted line) as small scales are dominated by resid@aB emission. When looking right through the galactic plane (red contour in Figure 1), residual noise (green dashed) is much higher on all clean (low) and dirty (high) galactic emission regions. The gray band shows the cales. For CMB-HD, any level of galactic emission leads to an increased noise on all scales.

> For reference in the gray band, we show the fiducial tSZ power spectrum along with 1σ2σ errors from SPT measurement (George et al. 2015). Comparing the gray band with noise curves, we note that all three surveys can map the peak of the

In addition to the instrumental noise and foregrounds, another source of noise for cluster detection is the confusion noise arising due to the diffuse tSZ signal. Note that the noise curve New is much lower than tSZ power spectrum for CMB-HD. While this indicates a high S/N measurement the tSZ power spectrum on all scales, it limits the sensitivity of cluster detection due to the tSZ confusion noise.

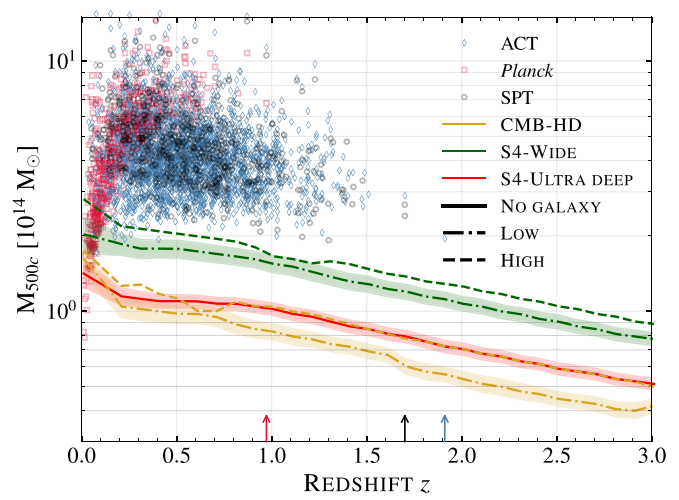
### 3.2. Baseline Results

Our baseline results with no modifications to the cluster tSZ signal are presented in Figures 3-5 and Tables 3 and 4.

### 3.2.1. Cluster Detection Sensitivity

Figure 3 shows the redshift dependence of the minimum cluster mass required to satisfy the detection threshold criterion S/N For referencewe also mark the clusters detected SaN from currentsurveys:ACT (Hilton et al. 2018, 2021) as blue diamond, Planck (Planck Collaboration et al. 2016b) as red squares, and SPT (Bleem et2al.15; Huang et al. 2020; Bleem et al. 2020) as black circles. We present two curves for CMB-HD (yellow) and S4-Wide (green): dashed-dotted and dashed curves correspond to sensitivity in regions dow and high levels of galactic emissionsespectively. For S4-Ultra deepsince we do not inject any galactic emissionwe only show the solid line containing no galactic foregrounds.

As expected, based on the intuition from Figure 2, minimum detectable cluster mass is lowest for CMB-HD followed by the variance for CMB-S4 surveys comes from the residuaCIB CIB levels can be lowered further. o this end, we altered the noise level of bands in both CMB-S4 surveys by modifying the



REDSHIFT *z*Figure 3. Cluster limiting mass threshold (S/N 5) as a function of redshift for future CMB surveys: CMB-HD in yellow, S4-Wide in green, and S4-Ultra deep in red. Different line styles correspond to the estimated sensitivity for different levels of galactic emission: solid for nodashed-dotted for lowand dashed for high galactic emissions, respectively. See Section 2.3.1 and Figure 2.2. for more details. Massesand redshifts of clusters with S/N currently available tSZ samples are also shown for comparis/60.T (Hilton et al. 2018, 2021) as blue diamonds, Planck (Planck Collaboration et al. 2016b)

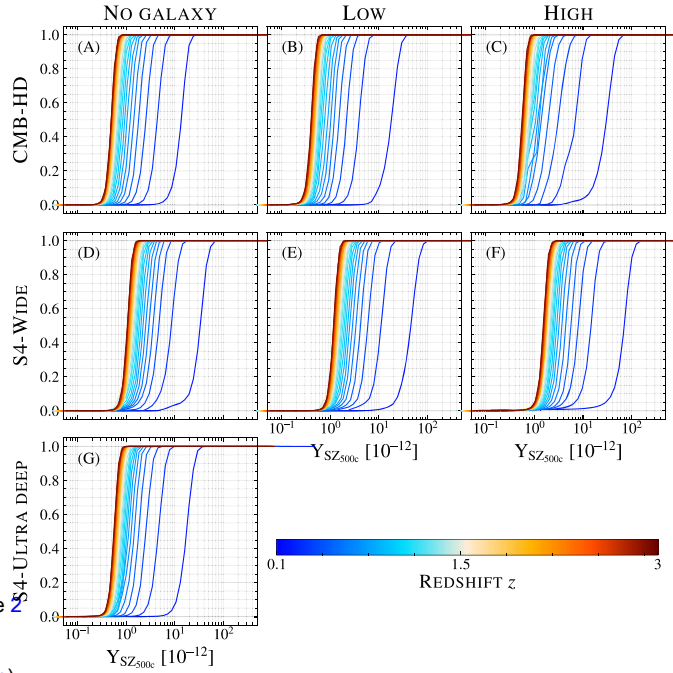
Figure 4. Cluster survey completeness as a function of integrated signal Figure 4. Cluster survey completeness as a function of integrated signal Figure 4. et al. 2020) as black circlesArrows represent the redshift of the most distant cluster discovered in each survey.

number of detectors in each band. We do not find any improvement, which suggests that the current configuration listed in Table 1 (CMB-S4 Collaboration 2019) is the most optimal for the CMB-S4 cluster survey.

For CMB-HD, since the residual CIB level is expected to be much lower than CMB-S4 in our setup (Sehgaet al. 2019), one could expect the cluster sensitivity to be much higher than with redshift is twofold. At low redshifts, the cluster S/N CMB-S4. However, the confusion noise from the diffuse tSZ (Holder et al. 2007) sets a noise floor hindering further improvementin sensitivity. Note that the gray signalband in Figure 2 is much higher than the noise culty for CMB-HD in yellow. The tSZ confusion noise can be lowered by masking compared to its low redshift counterpart. This leads to an the detected clustersout we defer a detailed investigation of this to a future work.

The sensitivity in regions of high galactic emission for S4-Wide is worse than the rest of the footprint by roughly 16% at all redshifts. For CMB-HD, the degradation is ~28% for clusters with z 1 and ~23% overall. While □30% S/N penalty is significant we note that it is an optimistic estimate given that our model for the galactic emission power spectrum (S0\_d0 dust and S0\_s0 from pySM3 simulations) is a simple power law. It ignores complexities like varying spectral or emissivity indices and non-Gaussianitieshich can introduce non-negligible biases to the cluster tSZ signas a result, we

While not shown in Figure 3, in the absence of galactic emission, cluster limiting masses reduce by ~7% compared to regions with low levels of galactic emission in the S4-Wide footprint. A significant fraction of this S/N degradation in the presence of galactic emission is for nearby clusters, in agreementwith excess large-scale noisegreen solid versus the spike atlow redshift in Figure 3 is because we limitS/N calculation to  $q_{\text{max}} = 2 \hat{q}$ . While  $2 \hat{q} > q_{000}$  for clusters with



for the three surveys with different levels of galactic emission. As expected, the curves indicate that surveys with lower instrumental noise and galactic foregrounds will allow us to detect clusters with lower  $Y_{\rm SZ_{500^{\circ}}}$  signals. The redshift trend is due to self-similar evolution of clusters and the residual contamination from CMB and atmospheric noise in the Compton-y maps.

 $z \square 0.5$  and hence optimal ur choice of  $q_{max}$  does not fully encompasthe cluster signal for nearby clustersand hence reduces their S/N.

The reason for the decrease in the minimum detectable mass degrades because of residuadntamination from atmospheric noise and CMB. At high redshifts, according to self-similar evolution of clusters (Kaiser 1986), a cluster with a given mass will have a higher temperature and hence a higher tSZ signal increase in cluster S/N when going from low to high redshifts.

### 3.2.2. Survey Completeness

Sensitivity can also be expressed in terms of cluster survey completeness as (Planck Collaboration ed. 2016b; Alonso et al. 2016)

$$c(Y_{SZ_{500^c}}) = \frac{1}{2} \left[ 1 + \text{ erf } \left( \frac{Y_{SZ_{500^c}}^{\text{true}} - q_{\text{lim}} s_{Y_{SZ_{500^c}}}}{\sqrt{2} s_{Y_{SZ_{500^c}}}} \right) \right], \quad (20)$$

where  $q_{\rm lim}=5$  is the detection threshold,  ${\rm sy}_{\rm SZ_{500c}}$  is the do not consider the clusters in regions of high galactic emission measurementuncertainty of the integrated  $Y_{SZ_{500c}}^{200c}$  signal for subsequent analyses in this work.

While not shown in Figure 3 in the absence of galactic Cluster limiting mass as a function of redshift shown in Figure 3 represents 50% survey completeness. In Figure 4, we show the completeness as a function of Y<sub>SZ<sub>5000</sub></sub> for all three the integrated Compton signalwithin the virial  $R_{500}$ . green dashed-dotted curves, in Figure 2. For all three surveys, Colors represent cluster redshift with z = 0 in blue and z = 3 in red. Higher experimental sensitivity will result in steeper curves. It will also push the curves to the left enabling detection

Table 3 Forecasted Number of Clusters from Future SZ Surveys with S/N 5 in Regions with Different Levels of Galactic Emission

Experiment		Baseline Footpri	nt		Dirty Footprint		Full Footprint		
	f <sub>sky</sub>	Total	z 2	f <sub>sky</sub>	Total	z 2	f <sub>sky</sub>	Total	z 2
CMB-HD	50%	325,860	11095	17%	76,165	1894	67%	402,025	12,989
S4-Wide		75,701	992		17,541	166		93,242	1158
S4-Ultra deep	3%	13699	341		К		3%	13699	341

of clusters with a lower signal. This is evident from the figure, where we note that urves move from lower to higher values of  $Y_{SZ_{500}}$  for increasing levels of galactic emission (left to right). The slopes of individual lines also decrease in the same orderWe note the same pattern when going from lownoise to high-noise surveys (CMB-HD → S4-Ultra deep → S4-Wide) and also from low to high cluster redshifts (blue to red). The redshifttrend is because of(a) S/N degradation for low redshift clusters due to residual contamination from atmospheric noise and CMB and (b) S/N improvement due to selfsimilar evolution for higher redshift clusters. The significant S/ N penalty for lowest redshifts  $z \square 0.3$  is due to the hard cutoff  $q_{\text{max}} = 2$  used for S/N calculation. See Section 3.2.1 for more discussion.

Based on these results, we find that S4-Wide shall detect (at 5σ) all galaxy clusters with an integrated Compton  $Y_{SZ_{500c}} \, \mathbb{I} \, 10^{-12} \, \text{at z}$ 1.5 over the large area survey footprint (f<sub>sky</sub>= 50%) as shown in panel (E) of Figure 4Furthermore, S4-Ultra deep shalldetect(at 5σ) all galaxy clusters with an integrated Comptor SZ<sub>Snoc</sub> 1 5 ′ 10 13 at z 1.5 over the delensing survey footprint  $(k_v = 3\%)$  shown in the bottom panel (G). The sensitivity of CMB-HD is roughly similar to S4-Ultra deep but over a large region f<sub>sky</sub> = 50% of sky as shown in panel (B).

#### 3.2.3. Cluster Counts

We present a cumulative redshift distribution of clusters expected from the three surveysin Figure 5: CMB-HD in yellow, S4-Wide in green, and S4-Ultra deep in red. Cluster counts are obtained by sampling Tinkeret al. (2008) HMF using the MC sampling approach discussed in Section 2.8.1. Dashed-dotted lines for CMB-HD and S4-Wide correspond to clusters expected from regions with low galactic foregrounds. Solid curves are the total number of clusters from the full footprint, i.e., a combination of both low and high galactic emission regions, and the split between the two regions can be of clusters in the baseline footprint from all three surveys. found in Table 3. Like in the previous Sections, galactic foregrounds are absent for S4-Ultra de€pr comparisonwe show the currently available SZ cluster samples (S/N 4.5) from ACT (Hilton et al. 2018, 2021) as blue dashed Planck (Planck Collaboration et al. 2016b) as red dotted, and SPT (Bleem et al. 2015, 2020; Huang et al. 2020) as black dasheddotted curves.

footprint (f<sub>sky</sub> = 50%) while the S4-Ultra deep will obtain ~14,000 clusters in CMB-S4's de-lensing footprint ( $f_{sky}$  = 3%). While most of the low redshift z  $\square$  1 clusters will be part of the LSST or eROSITA cluster samples(LSST Science Collaboration et al. 2009; Merloni et al. 2012), the

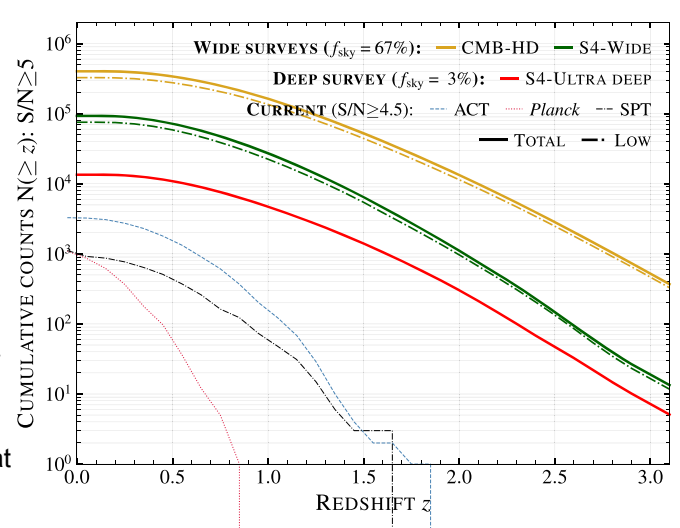


Figure 5. Cumulative cluster redshift distribution for future (current) SZ samples are shown as thick (thin) curves. For CMB-HD (yellow) and S4-Wide (green),we show two curves: dashed-dotted corresponds to clusters expected in the baseline (low galactic emission) footprint ( $f_{sky} = 50\%$ ) and solid corresponds to the total clusters expected in the combined low and high galactic emission region CMB-S4 is expected to detectlose to 1000 (350) clusters atz 2 in the baseline footprinf<sub>sky</sub> = 50%(3%) with the S4-Wide (S4-Ultra deep) survey. The number of z 2 is more than an order of magnitude larger for CMB-HD compared to CMB-S4. The enormous improvement in the sensitivity of high redshift clusters for future surveys compared to current experiments (thin lines) is evident from the curves.

redshift independen property of the tSZ signal will open the unique high redshift discovery space for future CMB surveys. For example, S4-Wide (S4-Ultra deep)'s expected to detect 1000 (350) clusters at z The number of clusters expected from CMB-HD is three times greater than that from S4-Wide. In the high redshift regime z 2,the expected number for CMB-HD is more than an order of magnitude higherthan CMB-S4. In Table 4, we give the median masses and redshifts Average lensing mass estimates of the cluster sample using both temperature and polarization CMB-cluster lensing is also given in the table. While CMB temperature returns a higher lensing S/N for S4-Wide, we find a polarization channelto dominate the S/N for S4-Ultra deep. This is due to the higher noise floor set by foreground signals along with additional S4-Wide shall detect close to 75,000 clusters in the baseline strategies used to mitigate foreground-induced bias in temperature-based lensing reconstruction. The same is true for CMB-HD but to a much lower extent since the variance from CIB is highly suppressed for CMB-HD (Sehgal et al. 2019). We report median mass and lensing estimates for both the full sample and also for clusters with z

Table 4 Median Mass and Redshift of Cluster Sample from the Future SZ Surveys in Their Baseline Footprint along with the CMB-cluster Lensing Mass Constraints

Experiment DM <sub>lens</sub> [10 <sup>14</sup> ]	z <sup>med</sup> M <sub>e</sub> ]			M <sub>500c</sub> [10 <sup>14</sup> M <sub>□</sub> ]		
		All	z 2	All	z 2	
CMB-HD	0.7	0.8	0.4	0.002	0.02	
S4-Wide	0.8	1.6	0.8	0.02	0.31	
S4-Ultra deep 0.7		1.0	0.6	0.05	0.55	

# 3.3. Change in Sensitivity due to Changes in Virialization

Modifying cluster virialization alters the cluster tSZ signal from clusters, which in turn affects the tSZ S/N. This is illustrated using the change in the minimum detectable cluster mass as a function of redshift in Figure 6 for S4-Wide with low model. The black curve is the baseline case for S4-Wide survey in the region levels of galactic emission. The thick solid black line is the baseline curvethe same as the green dashed-dotted curve in Figure 3. The thin dashed curves are for model 1 when we varyarameter ranging from nä [0.9 (blue), 1.1 (red)]. The thick pink dashed-the virialization officionesy from n ä [0.9 1.1] based on dotted curve is for model 2 with A = 0.155 and  $B_0 = 0.189$ . the virialization efficiency from  $\eta_v \ddot{a} [0.9, 1.1]$  based on Equations (11) and (12). As expected, the minimum detectable massesdecrease for  $h_v > h_v^{fid}$  (=1.0). The number of high redshift z 2 clusters from S4-Wide drop (increase) two times for  $\eta = 0.9(1.1)$  compared to 992 clusters for the fiducial value  $h_{v}^{\text{fid}} = 1.0$  (see Table 3).

Equation (13). It is similar to our baseline case (black), and we will provide sub-percent(0.5%) level constraints on we. For get roughly a 10% overallincrease in the number of clusters consistent with the trend in Figure 6.

# 3.4. Fisher Forecasts

Now we turn to parameter constraints using the Fisher formalism presented in Section 2.8We combine N(z,M<sub>1</sub>, q) with primary CMB information from the three surveys to forecast standard errors on the parameters governing one of the cale information from Planck has a negligible impaon the two virialization models along with the  $Y_{sz}$  - M scaling relation (Equation (9)) and cosmological parameters. For cosmology, we focus on two-parameter extension to Lambda cold dark matter (ACDM) to include the sum of neutrino masses∑m<sub>v</sub> and dark energy equation of state w<sub>h</sub>. Unless otherwise statedcluster counts N(zML, q) in the rest of this section includes temperature-and polarization-based CMBcluster lensing mass calibration he baseline redshift inning adopted was  $\Delta z = 0.1$  for  $0.1 _z < 1.5$  and one massive redshift bin for all high redshift clusters 1.5 \_ z \_ 3. A Planck-et al. 2019). Both experiments can provide sub-percent like prior has been assumed foroptical depth to reionization  $s(t_{re}) = 0.007$ .

We also look into the following: (a) individual constraints from primary CMB and cluster counts, (b) importance of CMB-cluster lensing-based mass calibration, (c) impact of high redshift clusters and redshift binning, and (d) the effect of  $t_{re}$ prior. These checks are limited to S4-Wide only.

### 3.4.1. Cosmology and Cluster Virialization Model

In Figure 7, we present the marginalized constraints (68% CL) on  $q\hat{1}$  [ $h_{v}$ ,  $b_{HSE}$ ,  $A_{v}$ ,  $B_{v}$ , å  $m_{n}$ ,  $w_{0}$ ] from all three surveys: CMB-HD in yellow, S4-Wide in green, and S4-Ultra deep in red. The lower and upper diagonals correspond to constraints for cluster virialization models 1 and 2espectively.

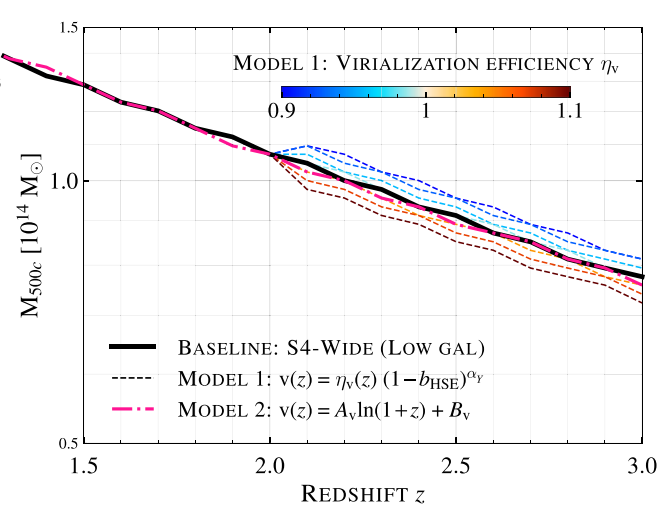


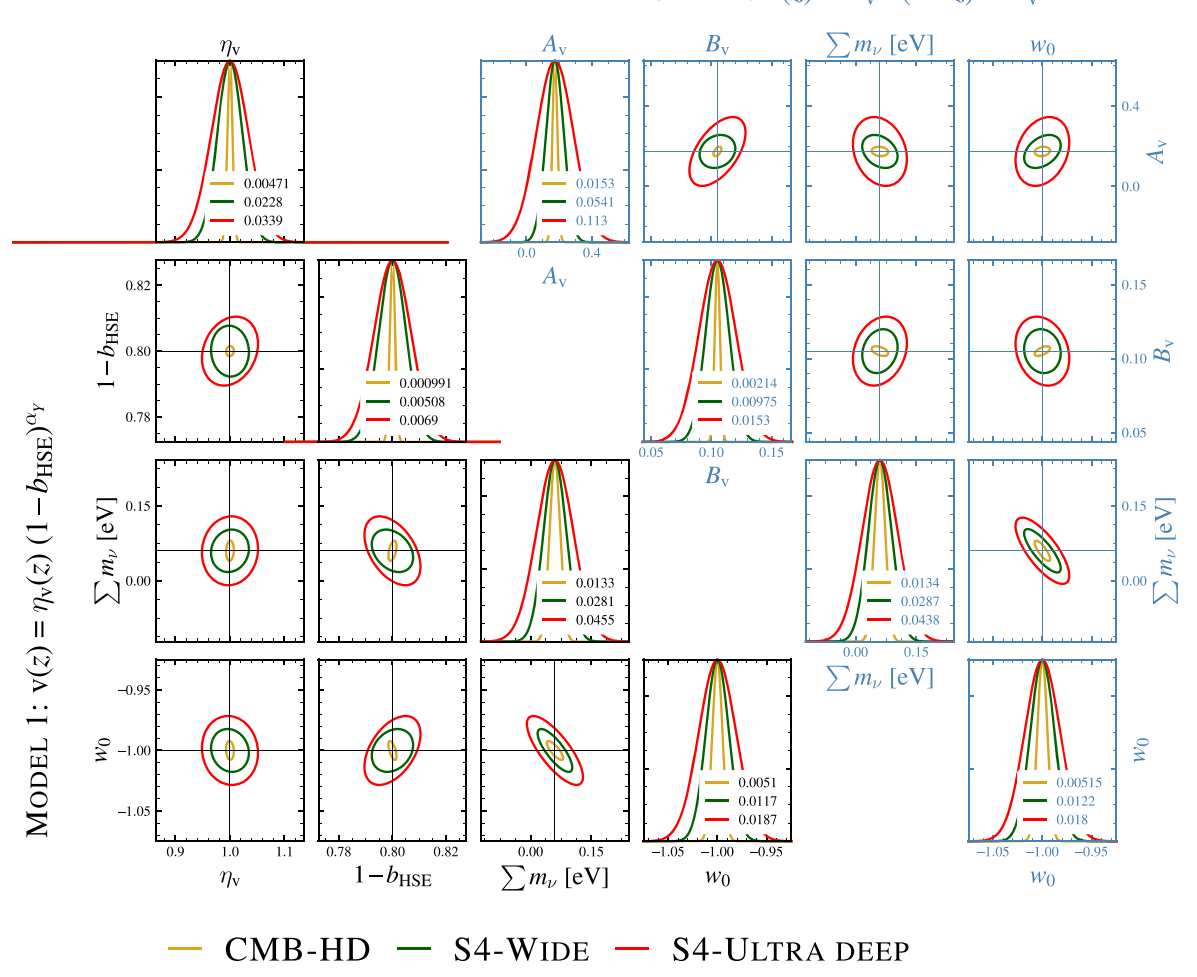
Figure 6. Dependence of cluster detection sensitivity on the virialization with low galactic emission, the same as the green dashed-dotted curve in Figure 3. The thin dashed curves are for model 1 with virialization efficiency

The CMB-S4 and CMB-HD experiments can provide stringent constraints on the dark energy equation of state  $\sigma(w_0)$  and the sum of neutrino massel we obtain 1%–2% on  $\sigma(w_0)$  from CMB-S4: 1.2% (1.8%) from S4-Wide (S4-Ultra The thick pink dashed-dotted curve is for model 2 based on deep) and 1% jointly from both CMB-S4 surveysCMB-HD neutrino masseswe obtain  $\sigma(\sum m_v) = 28 \text{ meV}(45 \text{ meV})\text{from}$ S4-Wide (S4-Ultra deep), 23 meV jointly from both, and 13 meV from CMB-HD, enabling a  $\sim 2.5\sigma - 4.5\sigma$  detection of the sum of neutrino masses from both CMB-S4 and CMB-HD assuming a normal hierarchy lower limit of 60 meV. Although not shown in the figures, both experiments provide □1% constraints on the scalar fluctuation amplitude As, Hubble parameter  $\sigma(h)$ , and dark matter density  $b^2\Omega$  Adding largeconstraints from S4-Wide and CMB-HD, while it improves the cosmological constraints from S4-Ultra deep by 5%-10%.

> Results for the first virialization model in Equation (11) are shown in the lower diagonal of Figure 7. We find that CMB-S4 clusters can help constrain  $\sigma(n)$  at the 2%-4% level, while CMB-HD can provide sub-percent level constraints. However, note that this assumes we have 100% knowledge abouthe astrophysics of low redshift clusters, which is not fully true but has been rapidly advancing (see recent review by Mroczkowski constraints on the HSE bias -  $b_{\rm HSE}$ . While  $\eta_{\rm v}$  only modifies the tSZ signal of clusters atz 2 and is only constrained by them, low redshift clusters are also important breaking the \_degeneraciesbetween other cosmological/scaling relation ˈparameters and√n For example,if we only consider clusters 2, ris highly degenerate with parameters like or σ<sub>8</sub>, and adding low redshift information almost entirely breaks the degeneracies with other parameters.

> The upper diagonal of Figure 7 shows the results for the second cluster virialization model in Equation (13). In this case, we obtain  $\sigma(A) = 0.05 (0.1)$  from S4-Wide (S4-Ultra deep) for the redshift evolution parameter the virialization, corresponding to ~33% jointly from the two CMB-S4 surveys. For  $\sigma(B_{\nu})$ , we get 5% and 8% from the two CMB-S4 surveys and

### MODEL 2: $v(z) = A_v \ln(1+z) + B_v$



15 z BINS:  $z \in [0.1, 1.5)$  ( $\Delta z = 0.1$ ) + [1.5, 3.0]; PRIOR(S):  $\tau_{re} = 0.007$ 

Figure 7. Marginalized Fisher constraints (68% CL) obtained by combining information from primary CMB spectra (TT/EE/TE) and cluster counts/\(\mathbb{L}\)(\bar{\mathbb{L}}\): CMB-HD is in yellow, S4-Wide in green, and S4-Ultra deep in red. We use a Planck-like (\hat{\mathbb{L}}\) (\hat{\mathbb{L}}\) = 0.007for all surveys. Both surveys can reduce the uncertainty on the dark energy equation-of-state parametes) (\hat{\mathbb{L}}\) (\(\mathbb{L}\)\) Combining primary CMB with clusters will also enable ~2.5\(\sigma -4.5\sigma\$ detection of the neutrino masses. The lower and upper diagonals representater virialization models 1 and 2respectively. Model 1: Cluster virialization efficiency \(\eta\$ can be constrained to an accuracy of 2\(\mathbb{L}\)-4\(\mathbb{L}\) by S4-Wide and S4-Ultra deep, while CMB-HD can provide sub-percent level constraints. All surveys provide <1\(\mathbb{L}\) constraints on the HSE bia parameter. Model 2: CMB-S4 can provide 33\(\mathbb{L}\) and ~4\(\mathbb{L}\) constraints \(\rho\) and \(\mathbb{L}\) \(\mathbb{L}\) parameters, while CMB-HD reduces the uncertainties on both parameters by three times Errors on other parameters do not change significantly between the two cluster virialization models.

~4% jointly. CMB-HD will reduce the measurementncertainty on these two parameters by more than three times.

Modifying cluster virialization from model 1 to model 2 does notintroduce statistically significant ifferences in other parameter constraints as can be seen by comparing the lower and upper diagonals in Figure 7.

#### 3.4.2. Observable-Mass Scaling Relation

The scatter in the  $g_{SZ}$  -  $g_{SZ}$  -  $g_{SZ}$  scaling relation is constrained to the 13%–16% level by CMB-S4, and to the 2% level by CMB-HD. The 1 $g_{SZ}$  errors on mass and redshiftvolution parameters of the relation are  $g_{SZ}(a_{\gamma})=0.01$ ,  $g_{SZ}(b_{\gamma})=0.02$ , and  $g_{SZ}(a_{\gamma})=0.02$  for S4-Wide. When switching from model 1 to model 2, we note a strong degeneracy between Med  $g_{SZ}(a_{\gamma})$  since they both probe the redshiftevolution of the tSZ signal. The mass and redshift evolution parameters of the log-normal scatter ( $g_{SZ}(a_{\gamma})$ ) are an order of magnitude worse. The numbers are similar or sometimes slightly better for S4-Ultra deep, which is because of a better lensing S/N per cluster for

S4-Ultra deep. We note that CMB-HD can improve constraints on the  $Y_{\rm sz}$  - M scaling relation parameters by roughly an order of magnitude compared to CMB-S4.

### 3.4.3.CMB versus Cluster Counts

In Figure 8, we present the constraints (68% CL) separately from CMB TT/EE/TE (orange dotted) and cluster counts (purple dashed) for S4-Wide. The green solid curves correspond to the joint CMB and cluster count constraints. As before, lower and upper diagonals correspond to virialization models 1 and 2. CMB spectra are insensitive to cluster virialization parameters ( $h_V$ ,  $h_{\rm HSE}$ ,  $A_V$ ,  $B_V$ ), and hence, the orange dotted curves are not shown for those parameters. However, CMB still helps in constraining them by breaking degeneracies with other parameteFbat is the reason for the difference between the purple dashed (cluster counts) and green solid (joint constraints) curves. For other parameters CMB spectra add minimal to modest levels of information compared to clusters. However, since CMB and cluster counts prefer

### MODEL 2: $v(z) = A_v \ln(1+z) + B_v$

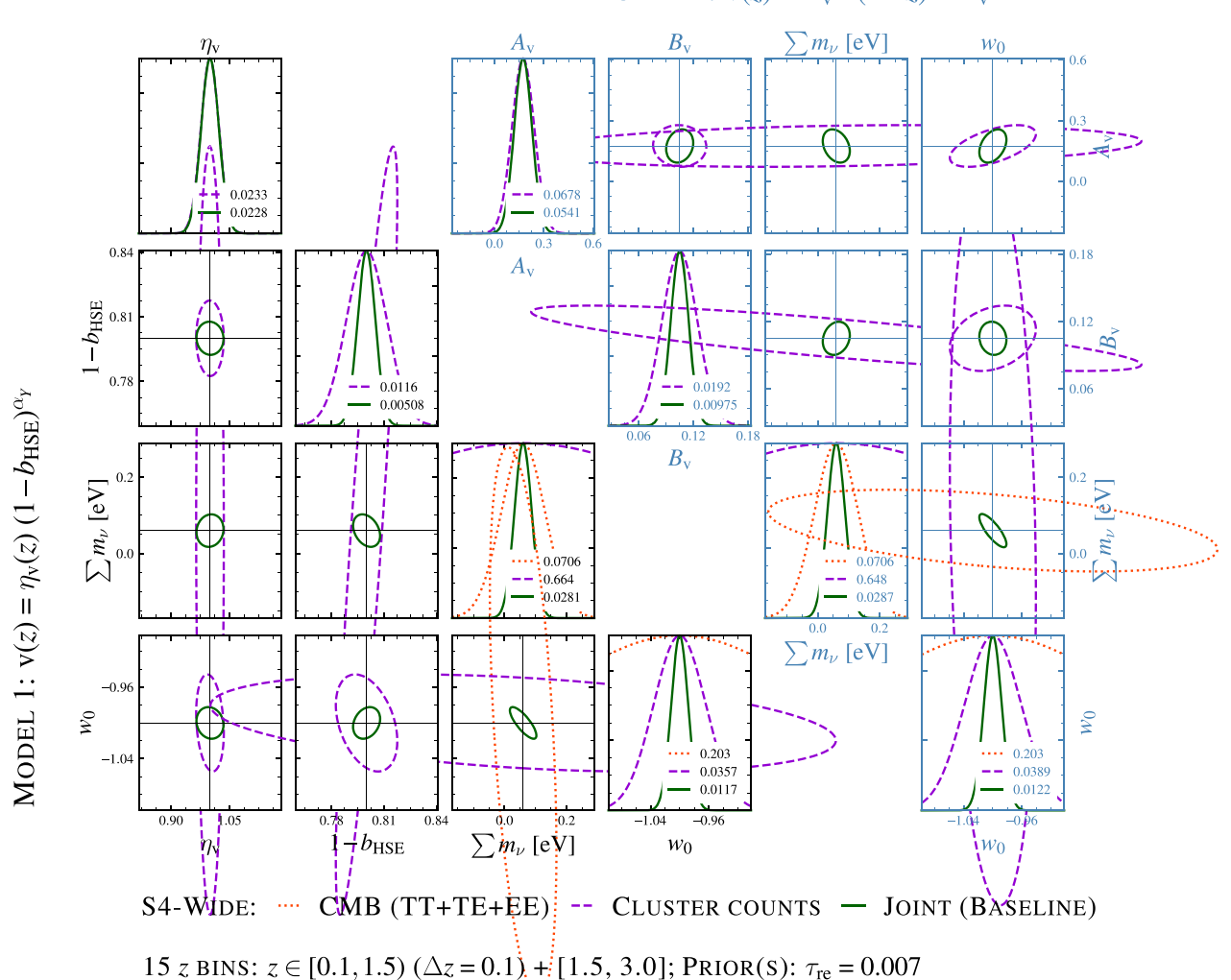


Figure 8. Individual constraints (68% CL) from CMB TT/EE/TE spectra (orange dotted) and cluster counts (purple dashed) are shown. The combination of the two, our baseline setup, is shown as the green solid curves. The nearly orthogonal degeneracy directions of CMB spectra and cluster counts on structure growth param provide excellent joint constraints compared to either of them individually on  $\sigma(\Sigma)$  and  $\sigma(W_0)$ . Only S4-Wide is shown.

different nearly orthogonal degeneracy directions the joint constraints offer remarkable improvements compared to either of them individually. For example, constraints on the sum of neutrino masses improve by  $\times 2.5$  from  $\sigma(\sum m_v) = 70$  meV to 28 meV, when adding cluster counts to primary CMB spectra.

#### 3.4.4. Importance of Lensing Masses

CMB-cluster lensing-based massalibration is critical to obtain the results described above. To highlight the importance pessimistic setting by ignoring clusters at z > 1.5. we present constraints with (green solid) and without (pink dashed)CMB-clusterlensing information in Figure 9. When CMB-cluster lensing in excluded, we simply bin clusters in tSZ in Figure 7). Constraints on other virialization model S/N q and redshift z: N(z, q). Since both cosmologicaland  $Y_{sz}$  - M scaling relation parameters affette cluster redshift and tSZ S/N distributions, they can be constrained even in the binning scheme has a negligible (<10%) impaot  $A_s$ ,  $\sum m_v$ , absenceof lensing massesalbeit rather weakly (Louis & Alonso 2017). For example, errors on cosmological parameters Case (ii): In this case, we see a threefold improvement in  $\sigma(\Sigma m_v)$  = 60 meV and  $\sigma(w_0)$  = 0.03 both degrade by more than two times for pink without lensing compared to green curves with lensing mass calibration Errors on virialization model parameters also degrade similarly by three times or more Case (iii): Since polly affects clusters with z without lensing mass information.

#### 3.4.5. Impact of High Redshift Clusters and Redshift Binning

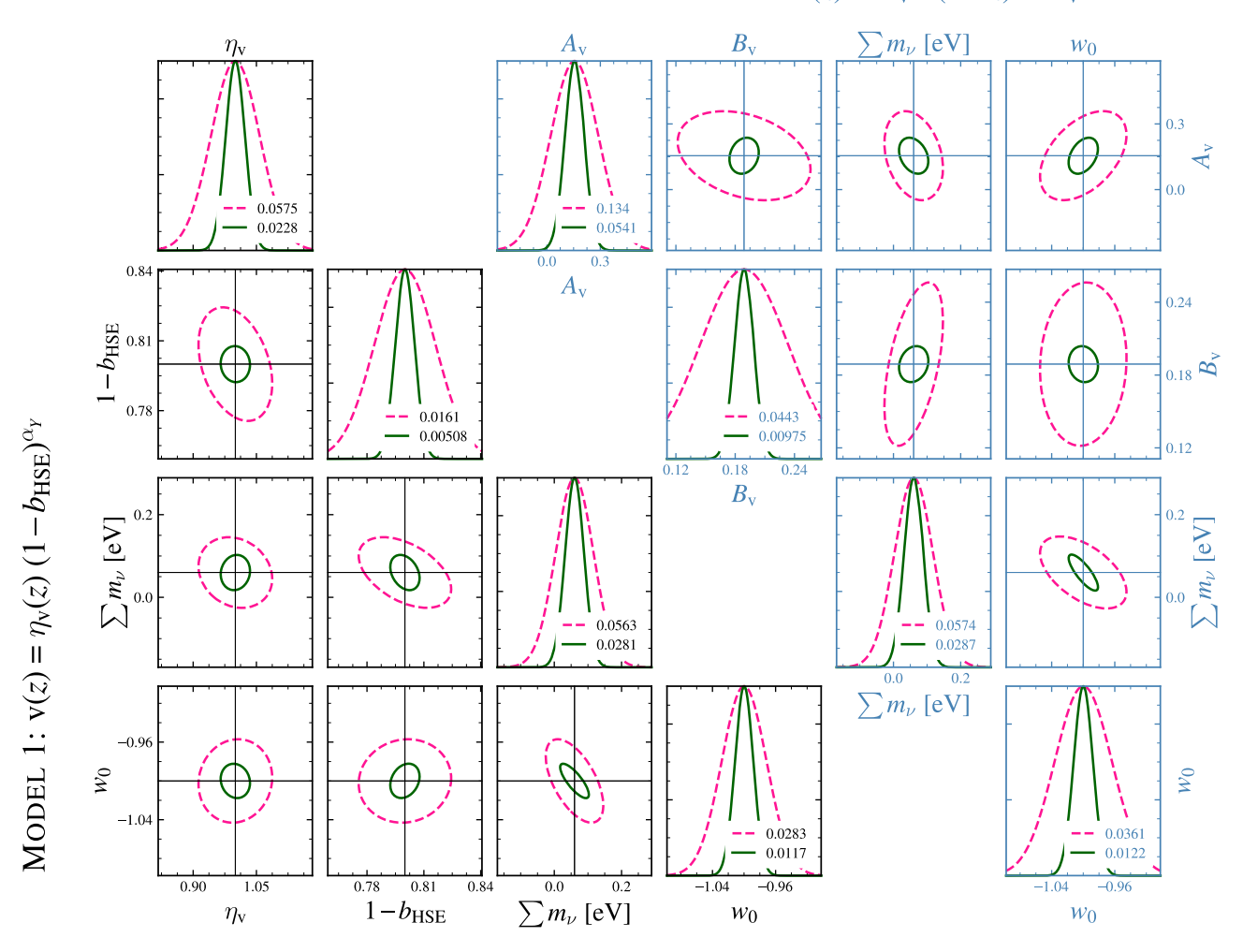
The constraints presented abovehave been derived by binning clusters atz 1.5 in one massive high redshiftin. This is a conservative approach to take into account the difficulty of obtaining redshifts for distant clusters. We modify this choice using: case (i) an optimal setting with  $\Delta z = 0.1$  for all clusters; case (ii) a less conservative setting with  $\Delta z = 0.1$ for  $0.1 \underline{\hspace{0.1cm}} z < 2$  and  $\Delta z = 1$  for  $2 \underline{\hspace{0.1cm}} z \underline{\hspace{0.1cm}} z$  3; and cas(eii) a

Case (i): We note a ×3.8 better constraint on the first on the constraint of the constraint on the constraint of the constraint on the con compared to the baseline case of (#) 0.0228 (see green curve parameter  $\mathcal{P}_{\text{\tiny HSE}}$ ,  $\mathcal{A}_{\text{\tiny V}}$ ,  $\mathcal{B}_{\text{\tiny V}}$  also improve by 20%–30%. Similar improvements are seen foh, wo but this optimistic redshift and  $\Omega h^2$ .

 $\sigma(\eta_v) = 0.0092$  and a 15% improvement on  $b_{HSE}$ ,  $A_v$ ,  $B_v$ compared to the baseline case, but this setting has a negligible (<10%) impact on other parameters.

2, we do not constrain gwith this pessimistic setting even though this is one

# MODEL 2: $v(z) = A_v \ln(1+z) + B_v$



S4-Wide: -- No CMB-cluster lensing — With CMB-cluster lensing (Baseline)

15 z BINS:  $z \in [0.1, 1.5]$  ( $\Delta z = 0.1$ ) + (1.5, 3.0); PRIOR(S):  $\tau_{re} = 0.007$ 

Figure 9. Importance of CMB-cluster lensing mass calibration for cluster counts. The green curves are the same in the left panels, while the pink dashed curves are constraints obtained without CMB-cluster lensing information. Ignoring lensing mass calibration degrades the constraints significantly for all parameters. Ellipses a 68% CL regions, and only S4-Wide is shown.

of the main goals of this work. Nevertheless we perform this test to address the challenges in obtaining redshifts and understanding the survey selection for clusterszat 1.5. We note up to 15% degradation in constraints on cosmological parametersindicating that clusters with z \_ 1.5 dominate cosmologicalconstraints. The other virialization model parameter constraints,  $b_{HSE}$  and  $B_v$  worsen by 15%, while  $A_v$ , controlling the redshift evolution of model 2, degrades by more  $s(t_{re}) = 0.002$   $\sigma(\sum m_v)$  improves by ×1.3–1.5 from the three than 60%.

### 3.4.6. Effect of $s(t_{re})$ Prior

Here we check the effect of the Planck-like prior adopted in the forecasts above. Since a higher optical depth would suppresssmall-scale CMB anisotropies,  $t_{re}$  has significant correlation with parameters like  $h_{,c}\Omega^2$ ,  $\sum m_{v}$ , and  $w_{0}$  and the choice of  $s(t_{re})$  prior can affect other parameter constraints. Subsequently we check the effect of replacing Planck  $s(t_{re}) = 0.007$  with (i) no  $s(t_{re})$  prior and (ii) a cosmic

variance limited measureme**s**t( $t_{re}$ ) = 0.002, for example as expected from the LiteBIRD or CORE satellites (Hazra at 2018; Di Valentino et al. 2018). Even though this has an effect on CMB-only constraints on all of the parameters listed above. we note significant effects only on  $\sum rand \Omega h^2$  with the joint CMB and cluster count information.

Removing  $t_{re}$  prior degrades  $\sigma(\sum m_v)$  by ×1.5. With surveys. We obtain a similar level of changes on of notice the two settings. The prior on  $t_{re}$  does not affect virialization model parameter constraints.

### 3.5. Dependence on Total Survey Time

Thus far, the forecasted clusternumber counts and the cosmological constraints are obtained using noise levels in Table 1 expected to be achieved at the end of survey periods. Given that S4-Wide is expected to start operations close to the end of this decade, these constraints may not be achieved until

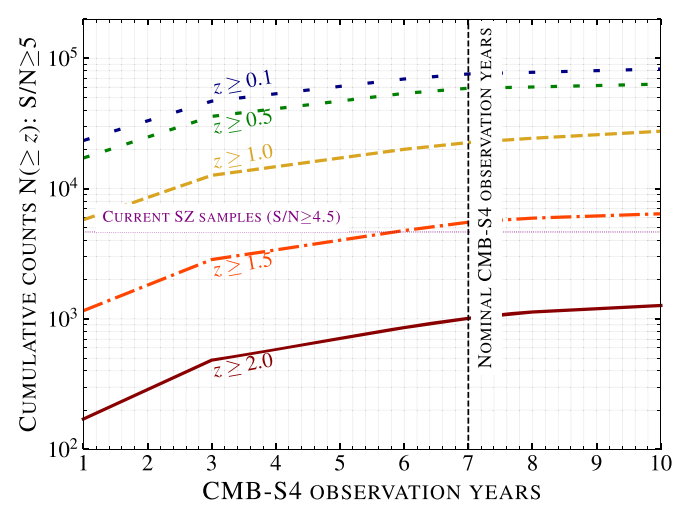


Figure 10. Cumulative clustercounts for S4-Wide shown as a function of number of observation years. The number of clusters in a 1 yr S4-Wide sample combining clusters with primary CMB as a function of S4-Wide observing will surpass the currently available SZ cluster samples (purple dashed-dotted years. Our results indicate tha 64-Wide can return remarkable cosmological 7 yr because ofresidual foreground signals that dominate smallscales and hence have a major impacon high-z clusters For example the actualz clusters at the end of the first year are two times lower than what will be obtained using a simple noise scaling

the middle of next decade. In this section, we check the dependence of cluster counts and cosmological constraints as light relic density and the production legacy catalogs in function of observing time for S4-Wide. For this test we simply millimeter/submillimeter wavelengthsthat require the proscale the noise levels in each band by  $N_{\text{years}}/N_{\text{baseline}}$  where N<sub>baseline</sub>= 7 yr. We go from 1 yr to 10 yr. Note that this simple scaling assumesfull deploymentat the start of the survey, which could be unrealistic, and the noise scaling may be slightly more complicated for the first few years in reality.

In Figure 10, we show the cumulative cluster counts for clusters above multiple redshifts as a function of the number of S4-Wide observation years. It is evident from the figure that the S4-Wide clustersample, with ~20,000 clusters, will surpass the currentSZ samples from ACT, Planck, and SPT (purple dotted line) even at the end of the first year of observation. fact, at the end of the first year, the S4-Wide sample will have close to 5000 clusters at 1 similar to the total number of current SZ clusters at all redshiftst is also worth noting that we use an S/N threshold of 5 for S4-Widewhile the current SZ samples shown here use 4.5.

The number of clusters expected at the end of each year ca be obtained from baseline results (7 yr)sing a simple noise scaling because of residual foregrounds in the Compton-y n Since the residual foregrounds (mostly CIB) dominate small scalesthe impact of residual foregrounds is more important for high redshift clusters that span a smaller angular extent on the seen identified in Planck clusters (Planck Collaborationæt For example scaling S4-Wide clusters at 2 from Table 3 should return $N_{\text{clus}}^{1 \text{ year}}(Z \square 2) = \sqrt{7} (992) = 375 \text{ clusters while}$ we have □200 clusters (two times lower) at the end of year 1 i □10% and showed that this contamination has a negligible Figure 10.

a function of S4-Wide observation years are presented in Figure 11. Similar to cluster forecasts, noise levels in each banguppressed (Popesso et al. 2015). Furtherntbæcluster tSZ are scaled from Table 1 for each year to obtain the CMB Fishesignal goes as M3 while DSFG signals are roughly linear. As matrix. The improvement in constraints is not dramatic as a function of observing years and this is primarily because of different degeneracy directions in the parameter space probed (M<sub>500c</sub>□ 10<sup>4</sup>M<sub>e</sub>) and high redshift z by clusters and primary CMB. However, note that cluster

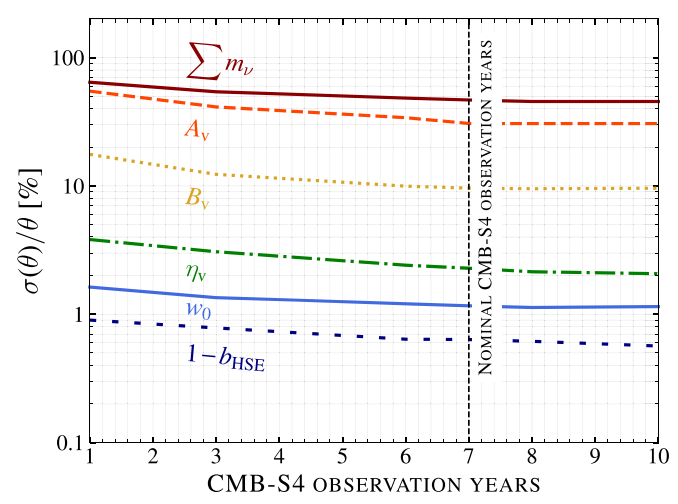


Figure 11. Relative cosmological constraints that can be obtained by line). The counts cannot be simply scaled from the baseline observing period of onstraints compared to current limits even in its first few years of observation. S4-Wide, at the end of the first few years of observations can also place compelling constraints on the virialization mechanism of high redshift clusters that is currently unconstrained.

cosmology is not the only science driver for CMB-S4. It has a broad range of science goals including the measurement posed N<sub>baseline</sub> = 7 yr (CMB-S4 Collaboration 2019) to produce wide and deep CMB maps. With ~200 (400) clusters 2 at the end of year 1 (3), we find that S4-Wide can make a giant leap toward understanding the astrophysicand the onsetof the virialization mechanism of high redshiftlusters, which are completely unconstrained currently.

# 3.6. Effect of Cluster Correlated Foreground Signals

In our baseline approach, we ignored cluster correlated foreground signals, namely the cluster kSZ signal and emission from DSFGs and RGs within clusters. For clusters close to detection limits for all three surveys considered hereluster kSZ signals are less important as they are expected to be much smaller than the tSZ signal. Moreover, kSZ can be both positive or negative depending on the direction of the radial motion and hence only acts as an additional source of variance in our analysis. On the other handemission from DSFG and os radio galaxies, since they are always positive, can fill in the tSZ decrements thereby potentially contaminating tSZ measurements. While the presence of DSFG signals within clusters has 2016d), Melin et al. (2018a) reported that signals from DSFGs degrade the completeness f the Planck cluster catalog by impact on cosmological parameterinference. However, the Cosmological constraints from clusters and primary CMB as Planck cluster sample deals with massive low redshift clusters where the star formation has been observed to be highly a result, DSFG contamination may be insignificant for Planck clusters. In this work, we are particularly interested in low-mass 1.5 clustersnear the peak of cosmic star formation history, to constrain cluster

astrophysicshence, dust contamination mightpotentially be important.

We check the impact of cluster correlated signals using Webskyltiple realizations of the millimeter-wave sky, as released (Stein et al. 2020) and MDPL2 (Y. Omori 2022, in preparation) recently by Han etal. (2021) using deep learning techniques, simulations. Webskysimulations are publicly available, while MDPL2<sup>15</sup> is currently under preparation and obtained using private communicationFor this test, it is important that the correlation between tSZ and CIB signals in Websky and MDPL2 simulations is in agreement with the measurements reported in the literature.Defining the correlation coefficient between the two  $as_{SZ}$ ,  $cib = \frac{C_\ell^{ISZ} \cdot cib}{\sqrt{C_\ell^{ISZ} \cdot isZ}C_\ell^{CiB} \cdot CiB}$ , the value for Websky (MDPL2) at  $\ell = 3000$  is ~0.25 (0.17). These are in reasonableagreement with the values reported by SPT Collaboration et al. 2016e). To this end, we extract 2° × 2° cutouts of kSZ and DSFG emissions around haloes in the masexplained above. We obtain zero false detections, which is and redshift grid used for S/N calculations:  $\log M_{500c} \hat{I}$ [13, 15.4]  $M_{\Box}$  with  $\log D^{M} = 0.1 M_{\Box}$  and z \(\text{a}\) [0.1, 3] with  $\Delta z = 0.1$ . Before extraction, we mask sources with flux at 150 GHz above  $\S_{50}$ ~ 6 mJy. We also apply a frequencydependent caling factor for Websky DSFG signals to match SPT measurements. At 150 GHz, this map scaling factor is 0.7 felation with a spectralndex  $\alpha_{dust}$  = 3.2 and  $\alpha_{radio}$  = -0.6 to to match Websky to SPT  $D_{\ell_{3000}}^{150}$  = 12nK<sup>2</sup> (Reichardtet al. 2021). No such scaling was applied to MDPL2 simulations. In 2015). Again, we do not see any false detections from DS both cases, we pick 100 cutouts for every point in the M z grid. Due to the availability of a single Websky/MDPL2 mock sky realization, the number of kSZ/CIB signals available for this test reduces significantly for clusters with mass  $M_{500c} \square 3 \times 10^4 M_e$  at  $z \square 2$ . Hence, we limit this test to clusters below this mass and redshift range. We inject the cluster correlated signals from Websky/MDPL2 into our simulations in all of the frequency bands along with cluster tSZ signal, experimentahoise, CMB and other astrophysical foregrounds described in Section 2.1 which are then passed through the ILC pipeline.

For high redshift (z note that DSFGs within clusters shift the tSZ-based cluster massesslightly lower. However, the bias is subdominant compared to statistical uncertainties at roughly the \_ for all three surveys. The bias is almostzero for low redshift clusters. As expected, cluster kSZ signals have a negligible impact on the recovered tSZ signals.

Both Websky and MDPL2 do not contain emission from RGs within clusters. Subsequently, we choose an extremely conservative test to assess the impact of RGs within clusters on order of magnitude higherfor the CMB-HD the recovered tSZ signals. We inject a constant flux of  $S_{150}$ = 0.1 mJy or 0.5 mJy for all clusters where the latter is scaled to other bands assuming a spectral index=c-0.6 (Everett et al. 2020). This test is limited to S4-Wide only. We mJy (0.5 mJy) can bias tSZ find that an  $S_{150} = 0.1$ measurements low by  $0.1-0.2\sigma$  ( $\square 1 \text{ W}$ ) hile a  $1\sigma$  systematic error is large, we note that our model for RGs is unrealistic, and HD. Given the importance of residual CIB signals and the the systematic error.

Websky simulations, which are currently being upgraded to include RG signals correlated with the underlying dark matter. galaxies, we use a simple constant flux model for all clusters.

Similarly the limitation due to the smaller number of Websky or MDPL2 haloes at the high-mass end can be addressed using for example. We leave these detailed studies for a future work.

#### 3.6.1. Impact on Sample Purity due to Point Sources

Given that point sources in the maps can be misclassified as

clusters, we check the effect of point sources using 100 noise-

only simulations. The simulations for this test include astrophysical foregrounds, CMB, experimental noise and point source signalsCluster tSZ signalis ignored here.We model the point source signals in three different ways. 0.2 ± 0.12 (George et al. 2015) and Planck 0.18 ± 0.07 (Planck In the first case, we add the cluster correlated DSFG signals in each mass and redshiftbin using Websky simulations as consistent with a negligible systematic bias from dusty sources estimated above in Section 3.6.In a similar spirit, we also check the effectof random pointsources in the mapsin this case, we inject point source signals with fluxes at 0.5, 1, 2, 3] mJy, which are then scaled to other bands using a power-law 2015). Again, we do not see any false detections from DSGFs. This indicates that DSFGs do not show up as 5σ positive peaks in the Compton-y maps. For radio point sources, we find that the sources with flux S <sub>150</sub> 2 mJy can be potentially problematic. However, these radio pointsources show up as negative peaks in the Compton-y maps and hence wolf be classified as clusters.

### 4. Conclusion

We forecasted the number galaxy clusters that can be detected using future CMB surveys, namely S4-Wide, S4-Ultra 1) clusters near the detection limit, wedeep, and CMB-HD. Our forecasts used realistic simulations that include signals from galactic and extragalactic signals along with atmospheric and instrumental noise components. In  $0.2\sigma$  levelhe baseline footprint with f  $_{\rm sky}$  = 50%, S4-Wide can detect dshift close to 75,000 clusters, and the CMB-HD sample will contain three times more clusters. The smaller but deeper S4-Ultra deep survey can detect ~14,000 clusters. Of these, 6000 (1500) will be at z 1.5, and 1000 (350) clusters will be at z 2 in the S4-Wide (S4-Ultra deep) cluster sample. The number of z experiment. Including regions close to the galactic plane ( $f_{skv}$  = 17%) increases the sample size by roughly 20%. roughly matches the point source sensitivity (3σ) at 90 GHz for The residual foreground signals, CIB in particular, dominate the CMB-S4 survey (CMB-S4 Collaboration 2019). The signal the small-scale variance in the Compton-y maps for CMB-S4. For CMB-HD, the variance from CIB is ×17 lower at 150 GHz due to efficient subtraction of dusty galaxy sources (Sehgal et al. 2019). The CIB subtraction and a five-times-smaller beam are the reasons for a much larger cluster sample from CMBhence our results should only be interpreted as an upper limit dtSZ × CIB correlation, we checked the systematic errors in the recovered clustertSZ signals due to emission from galaxies Our simple RG model can be potentially replaced using the within clusters. The effect of dusty star-forming galaxies was studied using Websky/MDPL2 simulations, while for radio Our results indicate that systematic error due to the presence of dusty galaxies is much smaller than the statistical error \_\_0.2σ, but having a constant radio galaxy signal with \$= 0.5 mJy

<sup>14</sup> https://mocks.cita.utoronto.ca/websky

<sup>15</sup> http://behroozi.users.hpc.arizona.edu/MDPL2/hlists/

can introduce ~1σ bias. The models used for galactic foregrounds and RGs are basic and must extended further. Nevertheless the tests we performed to assess the bontamsurveys.

We used a CMB-clusterlensing signalfrom both temperature and polarization to calibrate the cluster tSZ-mass scalingacknowledge supporfrom the facilities and staff of the Yale relation. We have ignored weak-lensing information from optical surveys in this work and note that cluding them can further improve the constraining powers well as act as an important systematic check for CMB-cluster lensing-based mass estimatesThe internally calibrated clustercounts were combined with primary CMB (TT/EE/TE) spectra to derive cosmologicalconstraints assuming a two-parameter extension to the standard model of cosmology ( $\Lambda$ CDM +  $\Sigma$ mw<sub>0</sub>). We show that the constraints on the dark energy equation-of-state associated with the Hoffman2 Shared Cluster provided by Ultra deep and sub-percent for CMB-HD. Similarly, the sum of Technology Group. neutrino masses∑m<sub>v</sub> can detected at □2.5σ-4.5σ by both CMB-S4 and CMB-HD surveys assuming a normal hierarchy lower limit of 60 meV. We also assess the importance of combining cluster counts with primary CMB significance of CMB-cluster lensingchoice of  $s(t_{re})$  prior, effect of different redshift binning, and dependence ofour result on the total survey time.

also study the evolution of the ICM using two modelsn the first case, we model cluster virialization in Equation (11) using the standard HSE bias parameter and a virialization efficiency parameter athat linearly scales with the tSZ signal from high redshift z 2 clusters We find  $\sigma(\eta_v) = 0.00471, 0.0228, and$ 0.0339 from CMB-HD, S4-Wide, and S4-Ultra deeprespectively, indicating that the mean deviation in thermal energy of 2 clustersfrom their low redshift counterpartscan be constrained to roughly 2%-4% by CMB-S4 and <1% by CMB-HD experiments. All three surveys can place sub-percent signal is reduced by constraints on the HSE bias paramet@ur second modeln Equation (13) is more physically motivated and calibrated using Omega500 hydrodynamical cosmological simulations. In this case, CMB-S4 can provide ~4% constraints on B, and  $\sim$ 33% on A  $_{\rm v}$ , which controls the redshift evolution of the virialization mechanismCMB-HD improves the constraining power by more than three timesThis work represents a key future CMB SZ surveys like AdvACT (Henderson et al. 2016), CMB-HD (Sehgal et al. 2019), CMB-S4 (CMB-S4 Collaboration 2019), SPT-3G (Benson et al. 2014; Bender et al. 2018), and SO (Ade et al2019). The binned cluster counts N(M<sub>1</sub>, g), Fisher matrices, and other associated productscan be downloaded.6

We thank the entire CMB-S4 collaboration<sup>17</sup> for helpful comments and suggestions throughout the course of this work. We further thank Neelima Sehgal for feedback on the manuscript; Sebastian Bocqueand Nikhel Gupta for useful discussions; and Yuuki Omori for providing access to MDPL2 simulations. Finally, we thank the anonymous referee for the useful suggestionsthat helped in shaping this manuscript

better. S.R. is supported by the Illinois Survey Science Fellowship from the Center for AstroPhysicaSurveys at the National Center for Supercomputing Applications. S.R. and N. ination on the recovered tSZ signals are important for future SZW. acknowledge support om NSF grants AST-1716965 and CSSI-1835865.S.R., N.W., G.H., and J.V. acknowledge support from NSF grant OPP-1852617.D.N. and H.A. Centerfor Research ComputingN.B. acknowledges support from NSF grant AST-1910021.E.P. is supported by NASA grant 80NSSC18K0403 and the Simons Foundation award No. 615662, as well as NSF grantAST-1910678.C.R. acknowledges support from the Australian Research Council's Discovery Projects scheme (DP200101068).J.V. acknowledges support from NSF under grants AST-1715213 and AST-1716127. This work used computational storage services σ(w<sub>0</sub>) parameter can be between 1% and 2% for S4-Wide/S4- UCLA Institute for Digital Research and Education's Research

# Appendix A Physically Motivated Cluster Virialization Model

Galaxy clusters are dynamically active objects and generally out of HSE due to mergers and mass accretion processes. lack of virialization is characterized by a nonthermalessure In addition to cosmology and scaling relation constraints, we fraction, P<sub>th</sub>/P tot, which quantifies the fraction of energy densities in unvirialized bulk and turbulent gas motions compared to the total pressure, $P_{tot} = P_{th} + P_{nth}$  (e.g., Lau et al. 2009; Battaglia etal. 2012; Nelson etal. 2014a; Shi & Komatsu 2014; Yu et al. 2015). In the presenceof the nonthermal pressurethe total pressure is given by the sum of the thermaland nonthermalpressure  $P_{tot} = P_{th} + P_{nth}$ , which in turn provides pressure support against gravitational collapse. Since the tSZ effectis sensitive to only the thermalpressure component  $Y_{tSZ} = Y_{tot} - Y_{nth}$ , the observed integrated tSZ

$$\frac{Y_{\text{nth}}}{Y_{\text{tot}}} = 1 - [h_{V}(Z)(1 - b_{\text{HSE}})^{a_{Y}}],$$
 (A1)

which represents the combination of the lack of virialization and HSE mass bias from Equation (9) and Y is the integrated pressure of each component within the sphere of R<sub>500c</sub> following Equation (6). Note that the nonthermalpressure is redshift clusters and the evolution of the ICM using current and the evolution of the ICM using the evolution HSE mass bias (e.gŅagai et al.2007b; Lau et al.2013; Shi et al. 2016; Biffi et al. 2016; Angelinelli et al. 2020).

> We compute the impacbf the nonthermalpressure on the  $Y_{\rm sz}$  - M relation of high redshift clusters using the model presented in Green et al. (2020). First, we use the analytical model of Shi & Komatsu (2014) to compute the evolution of nonthermal pressurey solving

$$\frac{ds_{\text{nth}}^2}{dt} = -\frac{s_{\text{nth}}^2}{t_{\text{dis}}} + h \frac{ds_{\text{tot}}^2}{dt}, \tag{A2}$$

where  $s_{\text{nth}}^2 = P_{\text{nth}}/r$  denotes the velocity dispersion due to nonthermal random motion,  $t_{\text{dis}}$  is the dissipation time of the turbulence scale  $t_{dis}$ ,  $s_{tot}^2 = P_{tot}/r$  is the total velocity dispersion, and n is the fraction of energy accreted thatis injected into turbulence motion. Due to the cosmic mass accretion process the total velocity dispersion increases over time. The turbulence decays into thermal energy over the

https://github.com/sriniraghunathan/tSZ\_cluster\_forecasts/

https://people.cmb-s4.org/public/showdir.php

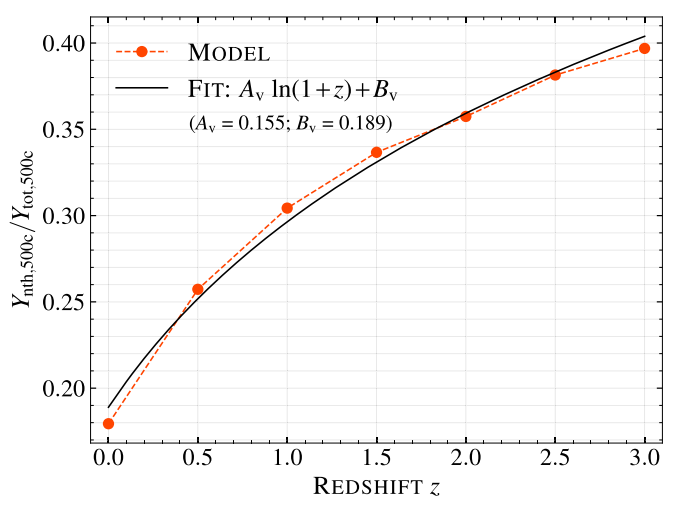


Figure A1. The ratio of the nonthermalpressure fraction  $Y_{nth}/Y_{tot}$  enclosed within the projected aperture radius of  $\partial_{c}$  for an  $M_{500c}$ =  $10^{14}\,M_{e}/h$  galaxy cluster as a function of redshift z. The model (orange) predicts that the nonthermalpressure increases as a function of redshiftue to the enhanced mass accretion rate in the early universe. We propose a fitting function (black solid), Equation (A3), which describes the redshift evolution out to z  $\approx$  3.

dissipation timescale  $t_{is}$ , which is proportional to the eddy turn-over time of the largest eddies, which is in turn proportionalto the local orbital time,  $t_{dis}(r) = \beta t_{orb}(r)/2$ . The model has been calibrated using Omega500 hydrodynamical cosmologicalsimulations (Nelson etal. 2014b), yielding the best-fit parameters of  $\beta = 1$  and  $\gamma = 0.7$  (Shi et al. 2015). Given a cluster with mass  $M_{5000}$  we generate the average mass accretion history M(t) and concentration c(t) of the cluster following van den Bosch et al(2014) and Zhao et al(2009), respectively For the total pressure profileswe use the KS01 (Komatsu & Seljak 2001) model, which is based on a polytropic gas in HSE with the NFW profile.

Figure A1 shows the fraction of the Y(< R<sub>500</sub>) signal in nonthermalpressure,Y<sub>ntt</sub>/Y<sub>tot</sub> as a function of redshift.For a constantmass M<sub>500c</sub>=  $10^{14}$ M<sub>e</sub>/h, the model predicts thatthe fraction of the Y signal in nonthermal pressure can evolve fron 20% at z = 0 to 40% at z = 3, indicating strong redshift dependence.The model predicts enhancement the nonthermal pressurefraction toward high redshift due to the enhanced mass accretion rate in the early universe (Green et 2020). Our result suggests that the evolution of Y<sub>ntt</sub>/Y<sub>tot</sub> at M<sub>500c</sub>=  $10^{14}$ M<sub>e</sub>/h can be described by a simple function:

$$\frac{Y_{\text{nth}}}{Y_{\text{tot}}} = A_{\text{v}} \ln(1 + Z) + B_{\text{v}}, \tag{A3}$$

where  $A_r$  and  $B_r$  are calibrated to 0.155 and 0.189.

#### ORCID iDs

Srinivasan Raghunathan https://orcid.org/0000-0003-1405-378X

Nathan Whitehorn https://orcid.org/0000-0002-3157-0407
Marcelo A. Alvarez https://orcid.org/0000-0002-2796-9650
Han Aung https://orcid.org/0000-0002-2153-6096
Nicholas Battaglia https://orcid.org/0000-0001-5846-0411
Gilbert P. Holder https://orcid.org/0000-0002-0463-6394
Daisuke Naga https://orcid.org/0000-0002-6766-5942
Elena Pierpaoli https://orcid.org/0000-0002-7957-8993

Christian L. Reichardt https://orcid.org/0000-0003-2226-9169 Joaquin D.Vieira https://orcid.org/0000-0001-7192-3871

#### References

```
Ade, P., Aguirre, J., Ahmed, Z., et al. 2019, JCAP, 2019, 056
Alonso, D., Louis, T., Bull, P., & Ferreira, P. G. 2016, PhRvD, 94, 043522
Angelinelli, M., Vazza, F., Giocoli, C., et al. 2020, MNRAS, 495, 864
Arnaud, M., Pratt, G. W., Piffaretti, R., et al. 2010, A&A, 517, A92
Artis, E., Melin, J.-B., Bartlett, J. G., & Murray, C. 2021, A&A, 649, A47
Battaglia, N., Bond, J. R., Pfrommer, C., & Sievers, J. L. 2012, ApJ, 758, 74
Baxter, E. J., Keisler, R., Dodelson, S., et al. 2015, ApJ, 806, 247
Bender, A. N., Ade, P. A. R., Ahmed, Z., et al. 2018, Proc. SPIE, 10708,
   1070803
Benson, B. A., Ade, P. A. R., Ahmed, Z., et al. 2014, Proc. SPIE, 9153,
   91531P
Biffi, V., Borgani, S., Murante, G., et al. 2016, ApJ, 827, 112
Bleem, L. E., Stalder, B., de Haan, T., et al. 2015, ApJS, 216, 27
Bleem, L. E., Bocquet, S., Stalder, B., et al. 2020, ApJS, 247, 25
Bleem, L. E., Crawford, T. M., Ansarinejad B., et al. 2022, ApJS, 258, 36 Bocquet, S., Dietrich, J. P., Schrabback T., et al. 2019, ApJ, 878, 55
Cardoso, J.-F., Le Jeune, M., Delabrouille, J., Betoule, M., & Patanchon, G.
   2008, ISTSP, 2, 735
Chluba, J., Nagai, D., Sazonov, S., & Nelson, K. 2012, MNRAS, 426, 510
CMB-S4 Collaboration 2019arXiv:1907.0447
Cromer, D., Battaglia, N., & Madhavacheril, M. S. 2019, PhRvD, 100, 063529
Datta, R., Aiola, S., Choi, S. K., et al. 2019, MNRAS, 486, 5239
de Haan, T., Benson, B. A., Bleem, L. E., et al. 2016, ApJ, 832, 95
Delabrouille, J., Betoule, M., Melin, J. B., et al. 2013, A&A, 553, A96
Di Valentino, E., Brinckmann, T., Gerbino, M., et al. 2018, CAP, 2018, 017
Everett, W. B., Zhang, L., Crawford, T. M., et al. 2020, ApJ, 900, 55
Fakhouri, O., Ma, C.-P., & Boylan-Kolchin, M. 2010, MNRAS, 406, 2267
Geach, J. E., & Peacock, J. A. 2017, NatAs 1, 795
Green, S. B., Aung, H., Nagai, D., & van den Bosch, F. C. 2020, MNRAS,
Gupta, N., Porciani, C., & Basu, K. 2020, arXiv:2003.09069
Gupta, N., Reichardt, C. L., Ade, P. A. R., et al. 2019, MNRAS, 490, 5712
Han, D., Sehgal, N., & Villaescusa-Navarro F. 2021, PhRvD, 104, 123521
Hazra, D. K., Paoletti, D., Finelli, F., & Smoot, G. F. 2018, JCAP, 2018, 016
HendersonS. W., Allison, R., Austermann, J., et al. 2016, JLTP, 184, 772
Hilton, M., Hasselfield, M., Sifón, C., et al. 2018, ApJS, 235, 20
Hilton, M., Sifón, C., Naess, S., et al. 2021, ApJS, 253, 3
Holder, G., Haiman, Z., & Mohr, J. J. 2001, ApJL, 560, L111
Holder, G. P., McCarthy, I. G., & Babul, A. 2007, MNRAS, 382, 1697
Hu, W., DeDeo,S., & Vale, C. 2007, NJPh,9, 441
Huang,N., Bleem,L. E., Stalder,B., et al. 2020, AJ, 159, 110
Itoh, N., Kohyama, Y., & Nozawa, S. 1998, ApJ, 502, 7
Kaiser, N. 1986, MNRAS, 222, 323
Komatsu, E., & Seljak, U. 2001, MNRAS, 327, 1353
Lau, E. T., Kravtsov, A. V., & Nagai, D. 2009, ApJ, 705, 1129
Lau, E. T., Nagai, D., & Nelson, K. 2013, ApJ, 777, 151
Laureijs, R., Amiaux, J., Arduini, S., et al. 2011, arXiv:1110.3193
Lewis, A., Challinor, A., & Lasenby, A. 2000, ApJ, 538, 473
Lima, M., & Hu, W. 2004, PhRvD, 70, 043504
Louis, T., & Alonso, D. 2017, PhRvD, 95, 043517
LSST Science Collaboration, Abell, P. A., Allison, J., et al. 2009,
   arXiv:0912.0201
MadhavacherilM., Sehgal,N., Allison, R., et al. 2015, PhRvL, 114, 151302
Madhavacheril, M. S., Battaglia, N., & Miyatake, H. 2017, Ph.P96) 103525
MadhavacherilM. S., Hill, J. C., Næss,S., et al. 2020, PhRvD, 102,023534
Mak, D. S. Y., & Pierpaoli, E. 2013, PhRvD, 87, 103518
Makiya, R., Hikage, C., & Komatsu, E. 2020, PASJ, 72, 26
Mantz, A., Allen, S. W., Ebeling, H., & Rapetti, D. 2008, MNRAS, 387, 1179
Mantz, A. B., Abdulla, Z., Carlstrom, J. E., et al. 2014, ApJ, 794, 157
Mantz, A. B., Abdulla, Z., Allen, S. W., et al. 2018, A&A, 620, A2
Melin, J.-B., & Bartlett, J. G. 2015, A&A, 578, A21
Melin, J. B., Bartlett, J. G., Cai, Z. Y., et al. 2018a, A&A, 617, A75
Melin, J. B., Bartlett, J. G., & Delabrouille, J. 2006, A&A, 459, 341
Melin, J. B., Bonaldi, A., Remazeilles M., et al. 2018b, JCAP, 2018, 019
Merloni, A., Predehl, P., Becker, W., et al. 2012, arXiv:1209.3114
```

Mroczkowski, T., Nagai, D., Basu, K., et al. 2019, SSRv, 215, 17

Nagai, D., Kravtsov, A. V., & Vikhlinin, A. 2007a, ApJ, 668, 1

```
Nagai, D., Vikhlinin, A., & Kravtsov, A. V. 2007b, ApJ, 655, 98
Navarro, J. F., Frenk, C. S., & White, S. D. M. 1996, ApJ, 462, 563
Nelson, K., Lau, E. T., & Nagai, D. 2014a, ApJ, 792, 25
Nelson, K., Lau, E. T., Nagai, D., Rudd, D. H., & Yu, L. 2014b, ApJ, 782, 107
Planck Collaboration, Ade, P. A. R., Aghanim, N., et al. 2014, A&A, 571, A12
Planck Collaboration, Ade, P. A. R., Aghanim, N., et al. 2016a, A&A,
  594, A27
Planck Collaboration, Ade, P. A. R., Aghanim, N., et al. 2016b, A&A,
  594, A24
Planck Collaboration, Ade, P. A. R., Aghanim, N., et al. 2016c, A&A,
  594, A13
Planck Collaboration, Adam, R., Ade, P. A. R., et al. 2016d, A&A, 596, A104
Planck Collaboration, Ade, P. A. R., Aghanim, N., et al. 2016e, A&A,
  594, A23
Planck Collaboration, Aghanim, N., Akrami, Y., et al. 2020a, A&A, 641, A6
Planck Collaboration, Akrami, Y., Ashdown, M., et al. 2020b, A&A, 641, A11
PopessoP., Biviano, A., FinoguenovA., et al. 2015, A&A, 579, A132
Raghunathar, Holder, G.P., Bartlett, J.G., et al. 2019a, JCAP, 2019, 037
Raghunathan$., Patil, S., Baxter, E., et al. 2019b, PhRvL, 123, 181301
Raghunathar, Patil, S., Baxter, E. J., et al. 2017, JCAP, 8, 030
Reichardt, C. L., Patil, S., Ade, P. A. R., et al. 2021, ApJ, 908, 199
Remazeilles, M., Delabrouille, J., & Cardoso, J.-F. 2011, MNRAS, 410, 2481
Rozo, E., Wechsler, R. H., Rykoff, E. S., et al. 2010, ApJ, 708, 645
```

```
Salvati, L., Douspis, M., & Aghanim, N. 2018, A&A, 614, A13
Sartoris, B., Borgani, S., Rosati, P., & Weller, J. 2012, MNRAS, 423, 2503
Sehgal, N., Aiola, S., Akrami, Y., et al. 2019, BAAS, 51, 6
Sehgal, N., Aiola, S., Akrami, Y., et al. 2020, arXiv:2002.12714
Shi, X., & Komatsu, E. 2014, MNRAS, 442, 521
Shi, X., Komatsu, E., Nagai, D., & Lau, E. T. 2016, MNRAS, 455, 2936
Shi, X., Komatsu, E., Nelson, K., & Nagai, D. 2015, MNRAS, 448, 1020
Stein, G., Alvarez, M. A., Bond, J. R., van Engelen, A., & Battaglia, N. 2020,
  JCAP, 2020, 012
Sunyaev,R. A., & Zel'dovich, Y. B. 1970, CoASP,2, 66
Tegmark, M. 1997, PhRvD, 56, 4514
Thorne, B., Dunkley, J., Alonso, D., & Næss, S. 2017, MNRAS, 469, 2821
Tinker, J., Kravtsov, A. V., Klypin, A., et al. 2008, ApJ, 688, 709
van den Bosch, F. C., Jiang, F., Hearin, A., et al. 2014, MNRAS,
   445, 1713
Viero, M. P., Reichardt, C. L., Benson, B. A., et al. 2019, ApJ, 881, 96
Vikhlinin, A., Kravtsov, A. V., Burenin, R. A., et al. 2009, ApJ, 692, 1060
von der Linden, A., Allen, M. T., Applegate, D. E., et al. 2014, MNRAS,
Yu, L., Nelson, K., & Nagai, D. 2015, ApJ, 807, 12
Zhao, D. H., Jing, Y. P., Mo, H. J., & Börner, G. 2009, ApJ, 707, 354
Zhao, H. 1996, MNRAS, 278, 488
Zubeldia, Í., & Challinor, A. 2019, MNRAS, 489, 401
```